ELSEVIER

J. Non-Newtonian Fluid Mech. 116 (2004) 205–234

Journal of Non-Newtonian Fluid Mechanics

www.elsevier.com/locate/jnnfm

Flow of a wormlike micelle solution past a falling sphere

Sheng Chen, Jonathan P. Rothstein*

Department of Mechanical and Industrial Engineering, University of Massachusetts, Amherst, MA 01003, USA

Received 15 May 2003; received in revised form 25 August 2003; accepted 29 August 2003

Abstract

With the increasing use of wormlike micelle solutions as rheological modifiers in many consumer products, the prediction of the behavior of these fluids has grown increasingly important in recent years. In this paper, the flow past a sphere falling at its terminal velocity through a column of a wormlike micelle solution is experimentally studied. The working fluid is an entangled wormlike micelle solution of 0.05 mol/l cetyletrimethylammonium bromide and 0.05 mol/l sodium salicylate dissolved in water. The rheology of the fluid is characterized in both shear and transient homogeneous uniaxial extension. Sphere-to-tube ratios of $a/R = 0.0625$ and $a/R = 0.125$ are investigated over a wide range of Deborah numbers. The drag on the sphere is initially found to decrease with increasing Deborah number because of shear thinning effects. As the Deborah number is increased, the establishment of a strong extensional flow in the wake of the sphere causes the drag to increase to a value larger than that of a Newtonian fluid with the same viscosity. At a critical Deborah number, the flow becomes unstable and fluctuations in the sedimentation velocity of the sphere are observed. Particle image velocity measurements are used to analyze the flow fields around the falling spheres. These measurements show the presence of a strong negative wake. For the unstable flows, the velocity flow field is observed to fluctuate between a negative and extended wake. Pointwise and full-field flow-induced birefringence measurements are used to track the evolution in the deformation of the wormlike micelle chains. Strong evidence is found that suggests that the flow instability is the result of a breakdown of the wormlike micelle network structure in the wake of the sphere. This breakdown is related to the filament rupture observed in the extensional rheology experiments.

Keywords: Sphere; Wormlike micelle solution; Viscoelastic; Flow instability; Negative wake

1. Introduction

The motion of a sphere falling through a viscoelastic fluid is one of the most heavily studied problems in experimental and numerical non-Newtonian fluid mechanics [1–3]. The flow is complex with regions of shear near the sphere and extension in the wake. Experimental measurements of the terminal velocity of a falling sphere can be easily made and several techniques have been developed which use the

* Corresponding author.
E-mail address: rothstein@ecs.umass.edu (J.P. Rothstein).

0377-0257/$ – see front matter © 2003 Elsevier B.V. All rights reserved.
doi:10.1016/j.jnnfm.2003.08.005

motion of spheres through viscoelastic fluids as both a rheometric and flow diagnostic tool. Examples range from falling ball viscometry to diffuse wave spectroscopy employing submicron spherical beads as microrheometry probes [4]. The motion of a sphere falling in a bounded cylinder of fluid has been chosen as a benchmark problem for numerical simulations [5]. The resulting numerical simulations have lead to a better understanding of constitutive relations and the development of improved computational methods [6,7].

Several excellent reviews of the numerical and experimental results exist [1–3] and the reader is encouraged to consult these sources for a more complete discussion of the existing literature. Only the most pertinent work will be described here. Until very recently, the experiments and numerical simulations reported in the literature focused on the sedimentation of spheres through viscoelastic polymer solutions and melts. With the growing use of surfactant solutions and associative polymers as viscosity modifiers in highly filled materials such as foodstuffs, paints and personal care products, a better understanding of the sedimentation of spheres through these fluids is needed.

Surfactants are molecules that consist of a hydrophilic head group and a hydrophobic tail. When dissolved in water they can spontaneously form several different types of self-assembling aggregates [8–10]. The size and shape of the resulting aggregate morphology can range from spherical micelles, to wormlike micelles to lamellae depending on surfactant and counterion concentration and interaction. Because of their extensive use in everything from additives in paints and detergents to enhanced oil recovery and pesticides, an enormous amount of research has been devoted to investigating the morphology, phase transitions, and shear and extensional rheology of different surfactant solutions [10–15]. Under the proper conditions, the micelles, resembling slender rods, can entangle and impart viscoelasticity to the fluid [12]. The behavior of wormlike micelles solutions is similar to that of polymer solutions and melts. The primary difference being that, unlike a covalently bonded polymer backbone, micelles are in a state of thermodynamic equilibrium with the solvent and are continuously broken and reformed under Brownian fluctuations. This leads to a broad and dynamic distribution of micelle lengths which can change under an imposed shear or extensional flow [16].

In the regime of linear deformation imposed by small amplitude oscillatory shear flows, the response of many wormlike micelle solutions can be accurately modeled by a Maxwell model having just one or two relaxation times making these model fluids for rheological research [10]. Cates proposed that, in the fast breaking-limit, $\lambda_{break} \gg \lambda_d$, the relaxation time or a wormlike micelle solution, $\lambda = (\lambda_{break}\lambda_d)^{1/2}$, is a function of the reptation or disentanglement time of the micelle in solution, λ_d, and the characteristic time for the micelle to break and reform, λ_{break} [12]. The nonlinear viscoelastic response of these entangled micelle solutions has been shown to be much more complex. Several constitutive models have been developed specifically for entangled wormlike micelle solutions [17], although, models developed to describe the behavior of polymer solutions and melts such as the Giesekus model have been shown to predict the nonlinear viscoelastic behavior of wormlike micelles very well [15].

Filament stretching studies have recently shown that wormlike micelle solutions exhibit significant strain hardening and a breakdown of the stress-optical rule in transient homogeneous uniaxial extensional flows [15]. Rothstein [15] showed that a quantitatively fit to the extensional rheology of these wormlike micelle solutions could be achieved with a multimode FENE-P model having as few as two relaxation modes. At a critical stress, nearly independent of strain rate, the wormlike micelle solutions filaments were found to fail through a dramatic rupture near the axial midplane. The filament failure was not the result of elastocapillary thinning, but rather Rothstein [15] hypothesized that the failure stemmed from the local scission of individual wormlike micelle chains and a breakdown of the entangled micelle network

structure. The continuously evolving wormlike micelle network structure has been shown to lead to other interesting flow instabilities in the past.

Measurements of wormlike micelle solutions in a cone-and-plate, parallel-plate and Couette rheometer have demonstrated a shear thickening behavior followed by the onset of a flow instability [18–20]. Careful studies have been performed using stress measurements, birefringence and small angle light scattering to try and understand the shear thickening mechanism. Several explanations for the observed shear thickening have been proposed including shear-induced structure formation, shear-induced phase change from an isotropic to a nematic state and shear-induced transition to a gel-like state [18–20]. Shear-induced structure formation can also lead to a demixing of the surfactant solution and the formation of banded structures or slip layers of different surfactant morphologies with dramatically different rheological properties [21–23].

Jayaraman and Belmonte [24] observed an instability in the sedimentation velocity of a sphere falling through a 9 mmol/l CTAB and 9 mmol/l NaSal wormlike micelle solution. With the exception of the measurements of Bisgaard [25] which showed a fluctuating velocity in the wake of a sphere falling through a polyacrylamide solution at high Deborah number that was never independently reproduced, no other low Reynolds number elastic flow instabilities have been observed for a sphere falling through a polymer solution or melt. It can be concluded that the instability observed by Jayaraman and Belmonte [24] must, therefore, be a function of a stress-induced evolution of the entangled wormlike micelle network structure. We will show that the evidence from detailed experimental measurements of the flow field past falling sphere suggest that this new flow instability is likely the result of a breakdown of the wormlike micelle network structure in the strong extensional flow in the wake of the sphere and that this instability is related to the filament rupture observed in the extensional rheology experiments of wormlike micelle solutions.

The outline of this paper is as follows. In Section 2, we briefly describe the experimental setup, the implementation of several measurement techniques including flow-induced birefringence (FIB) and digital particle image velocimetry (DPIV) and the shear and extensional rheology of the wormlike micelle solution used. In Section 3 we discuss the experimental results and in Section 4 we conclude.

2. Experimental

2.1. Flow geometry and experimental setup

A schematic diagram of the flow geometry and experimental setup is shown in Fig. 1. The micelle solution was contained in an acrylic cylinder 91.4 cm in length and with an inner diameter of 10.2 cm. A rectangular acrylic viewing box with an inner side length 13.0 cm was co-centered with the cylinder. A glycerol and water solution was prepared with the same index of reflection as the cylinder and was used to fill the gap between the cylinder and the viewing box to eliminate light refraction at the acrylic–air interface. A ray tracing algorithm was used to remap the radial position and velocity of the vectors calculated through DPIV to account for the small index of refraction mismatch between the acrylic flow tube and the wormlike micelle solution.

The spheres were held below the fluid surface and released by a three pronged drill chuck which was precisely centered within the flow cylinder by a micrometer driven three-axis translation stage. The sedimentation velocity was varied by using a series of six spheres with a wide variation of densities. The spheres were composed of delrin (DL), Teflon (TF), aluminum (AL), aluminum oxide (AO), stainless

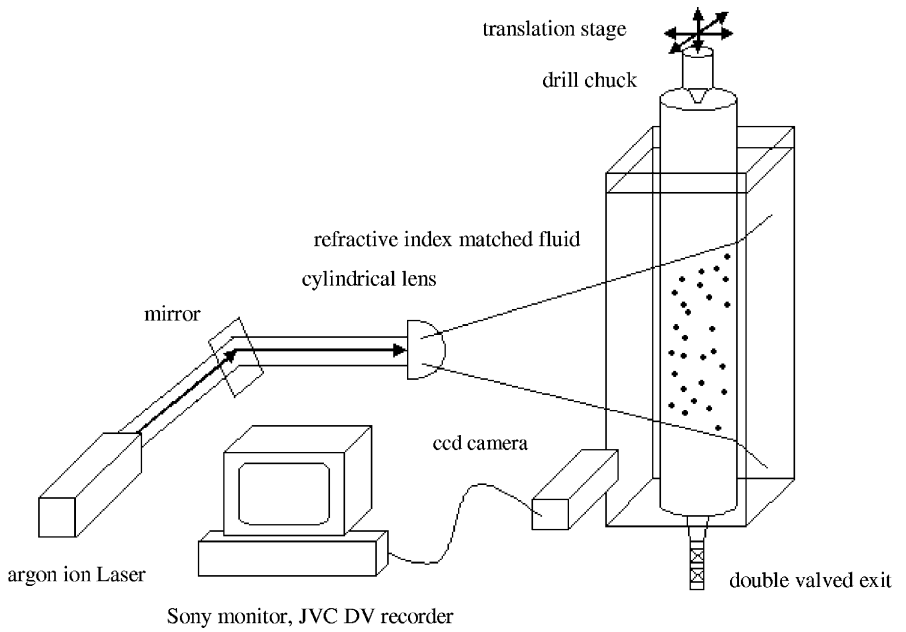

Fig. 1. Schematic diagram of experimental setup.

steel (SS), and tungsten carbide (TC) (Small Parts). The densities listed in Table 1 were determined by measuring the diameter and the mass of each sphere. Experiments were performed with spheres having diameters of $a = 6.325$ and 12.65 mm resulting in sphere to flow cylinder sphere-to-tube ratios of $a/R = 0.0625$ and 0.125.

2.2. Digital particle image velocimetry (DPIV)

DPIV was used to generate a complete and quantitative measurement of the velocity flow field around each of the falling spheres. The wormlike micelle solution was seeded with 45 μm, silver coated, glass spheres (Potters Industries) having a density of $\rho = 1100\,\text{kg/m}^3$. Although the tracer particles are more dense than the surrounding fluid, because of the high viscosity of the micelle solution and the small size

Table 1
Density and resulting Deborah number for each of the sphere materials and sizes used

Material	Density [kg/m^3]	Reynolds number, $Re(\dot{\gamma})$ $(a/R = 0.0625)$	Deborah number, De $(a/R = 0.0625)$	Reynolds number, $Re(\dot{\gamma})$ $(a/R = 0.125)$	Deborah number, De $(a/R = 0.125)$
DL	1.39×10^3	6.2×10^{-6}	0.23	4.0×10^{-4}	0.37
TF	2.14×10^3	4.9×10^{-5}	1.8	1.8×10^{-3}	1.7
AL	2.73×10^3	4.1×10^{-5}	1.5	3.0×10^{-3}	2.7
AO	3.94×10^3	6.6×10^{-5}	2.5	4.1×10^{-3}	3.8
SS	7.98×10^3	1.1×10^{-4}	4.0	7.5×10^{-2}	33
TC	1.51×10^4	1.7×10^{-4}	6.6	6.0×10^{-1}	110

of the seed particles, their settling time was calculated to be on the order of months. The tracer particles were mixed at 0.0025 wt.% resulting in a seed density of approximately 60 particles per cubic centimeter. For the field of view used in these experiments, this seed density is sufficient for acquiring excellent DPIV vector fields [26,27].

A measurement plane 35 cm from the bottom the flow cylinder and coinciding with the centerline of the sphere was illuminated with a laser light sheet formed by passing a 500 W argon laser (National Laser) through a cylindrical lens. The sheet thickness was found to be approximately $w \approx 1$ mm. The light scattered from the tracer particles was imaged with a CCD camera (Hitachi KPM22N) and recorded at 30 frames/s using a digital VCR (JVC SR-VS20U) with a resolution of 720 pixels × 480 pixels. The images were captured on a PC using video acquisition card (Pinnacle DV200) and processed using Adobe Premiere. A DPIV algorithm was used to determine the fluid velocity vector field by cross-correlating seed particle displacements in sequential images [28,29]. Length scale and velocity conversions from the pixel images to nondimensional values were made by measuring the sphere size as it passed within the field of view of the camera.

2.3. Flow-induced birefringence (FIB)

The refractive index of a wormlike micelle is different in the directions parallel to and normal to the micelle tube. FIB measurements have been used quite extensively to examine both steady and transient flows of and wormlike micelles [20,22,30–32]. By passing light of a known polarization state and frequency through the polymeric fluid sample and measuring the resulting change in polarization state, FIB can be used to determine the local anisotropy in the conformation of the wormlike micelles $\Delta A = A_{11} - A_{22}$ [30]

$$\frac{\Delta n' \cos 2\chi}{C} = G_{\mathrm{N}}^{0}\, \Delta A, \tag{1}$$

where $\Delta n'$ is the measured birefringence, χ the extinction angle, C the *stress-optical coefficient*, and G_{N}^{0} the plateau elastic modulus of the fluid. The micelle conformation is characterized by the ensemble average second moment tensor, $\boldsymbol{A} = \langle QQ \rangle / Q_{\mathrm{eq}}^{2}$ which is made dimensionless by the square of the equilibrium value of the end-to-end vector of the polymer chain, $\boldsymbol{Q}$. A modulated FIB technique [33,34] was utilized for both the extensional rheology measurements and for pointwise birefringence measurements in the wake of the falling sphere while the Osaki technique [30] was used to facilitate full-field birefringence measurements of the falling sphere.

The advantages of using a modulation technique over a full-field technique include significantly better spatial and temporal resolution and the ability to simultaneous measurement both the birefringence and the extinction angle with no ambiguity in orientation of the micelle [30]. The optical train used to measure the time evolution of the FIB at the midpoint of a wormlike micelle fluid filament experiencing a homogeneous uniaxial extension is similar to the system first proposed by Frattini and Fuller [35] and described in [33,34]. The retardation, δ, and the extinction angle, χ, can be calculated directly from the first and second harmonic of the modulated laser intensity captured by the photodetector

$$\delta = \frac{2\pi\, \Delta n'\, d}{\lambda_{\mathrm{light}}} = \cos^{-1}\left(\frac{-M_{32}^{2} \pm M_{34}^{2}\sqrt{1 - M_{34}^{2} - M_{32}^{2}}}{M_{34}^{2} + M_{32}^{2}} \right), \qquad \chi = \frac{1}{2}\cos^{-1}\left(\frac{M_{34}}{\sin\delta} \right). \tag{2}$$

where δ is the optical path length of the light, λ_{light} the wavelength of the laser light and M_{34} and M_{32} are the components of the Mueller matrix given by

$$M_{34} = \frac{I_\omega}{\sqrt{2}J_1(A_c)I_{dc}}, \qquad M_{32} = \frac{I_{2\omega}}{\sqrt{2}J_2(A_c)I_{dc}}. \tag{3}$$

In the above equation, A_c is the amplitude of the electro-optical modulation calibrated such that the order zero Bessel function of the first kind is equal to $J_0(A_c) = 0$ [35] and the intensity of the light measured by the photodetector is given by

$$I(t) = I_{dc} + I_\omega \sin \omega t + I_{2\omega} \cos 2\omega t. \tag{4}$$

For both the uniaxial deformation imposed by the filament stretching rheometer and the pointwise measurements along the centerline or the falling sphere, the orientation angle is found to be aligned along the axis of the falling sphere, $\chi = 0$, and thus $M_{32} \approx 0$. The minimum resolvable retardation of this modulated system is approximately $\delta \approx 1 \times 10^{-2}$ rad.

FIB has typically been used only in two-dimensional flows because it is a line-of-sight technique. In the three-dimensional or axisymmetric flows such as the flow past a falling sphere, the kinematics and the molecular conformation of the wormlike micelle vary along the path of the light resulting in an spatially averaged measure of the FIB. The pioneering work in this area was performed by Li and Burghardt [36] who investigated the axisymmetric stagnation flow of a high molecular weight polystyrene solution past a cylindrical obstruction with a hemispherical cap. Li and Burghardt [36] demonstrated that even though a spatially resolved measurements of birefringence, $\Delta n'(r, z)$, extinction angle, $\chi(r, z)$, and polymer conformation field $\Delta A(r, z)$ could not be achieved, axisymmetric flow-induced birefringence (AFIB) is an excellent tool for comparison between the results of numerical simulations and experiments [36–38]. To perform such a comparison in inhomogeneous flows, the conformations and stresses in the flow field upstream and downstream of a contraction–expansion can be numerically computed using a chosen constitutive model. It has also been demonstrated by Rothstein [39] that AFIB is an excellent tool for qualitative analysis of conformation and stress growth in complex flows of polymer solutions even in the absence of a direct comparison to numerical simulations.

Following the procedure outlined by Li and Burghardt [36] we can write down an expression for the spatially averaged version of Eq. (3)

$$\begin{aligned}
\bar{M}_{34} &= \sin\bar{\delta}\cos 2\bar{\chi} = \frac{1}{d}\int_0^d \sin\left(\frac{2\pi\,\Delta n'(x)d}{\lambda_{\text{light}}}\right)\cos(2\chi(x))\,\mathrm{d}x, \\
\bar{M}_{32} &= [1-\cos\bar{\delta}]\sin 2\bar{\chi}\cos 2\bar{\chi} = \frac{1}{d}\int_0^d \left[1-\cos\left(\frac{2\pi\,\Delta n'(x)d}{\lambda_{\text{light}}}\right)\right]\cos(2\chi(x))\sin(2\chi(x))\,\mathrm{d}x,
\end{aligned} \tag{5}$$

where x is the position along the path of the light passing through the birefringent material, $\bar{\delta}$ and $\bar{\chi}$ are spatially averaged values of the retardation and extinction angle, and $\bar{M}_{32}$ and $\bar{M}_{34}$ are the spatially averaged Mueller matrices. Deconvoluting Eq. (5) in order to calculate local measures of $\Delta n'(r, z)$, and $\chi(r, z)$ is an ill-posed problem, although it has been attempted in the past [40].

To obtain full-field FIB measurements of the spheres settling through a wormlike micelle solution, the Osaki method was used [30]. In order to acquire information about both the retardation and the extinction angle, the Osaka method requires FIB measurements from two different crossed polarizer arrangements. A single wavelength light source was used to illuminate the flow between crossed polarizers. A CCD camera

connected to digital VCR was then used to capture the fringe patterns in the wormlike micelle solution generated by the falling sphere for each linear polarizer configuration. The images were uploaded to a PC from the VCR and then processed to determine the spatially averaged retardation and extinction angle of the wormlike micelle solutions. To achieve a quantitative measure of the retardation, the background signal of the CCD camera was first subtracted from each image and the intensity was normalized with the light intensity in the absence of the linear polarizers to generate the following two normalized intensities:

$$i_{0^\circ} = \frac{2I_{0^\circ}}{I_{0,0^\circ}} = \sin^2(2\bar{\chi})\sin^2\left(\frac{\bar{\delta}}{2}\right), \qquad i_{45^\circ} = \frac{2I_{45^\circ}}{I_{0,45^\circ}} = \cos^2(2\bar{\chi})\sin^2\left(\frac{\bar{\delta}}{2}\right). \tag{6}$$

These two intensities were then manipulated to generate a full-field description of the spatially averaged values of the retardation and the extinction angle

$$|\bar{\delta}| = \sin^{-1}\sqrt{i_{0^\circ} + i_{45^\circ}}, \qquad |\bar{\chi}| = \frac{1}{2}\tan^{-1}\sqrt{\frac{i_{0^\circ}}{i_{45^\circ}}}. \tag{7}$$

Note that the sign of the retardation and extinction angle calculated using the Osaki method is ambiguous. The resolution of this full-field technique is limited by CCD camera to about $\delta \approx 0.1$ rad, an order of magnitude less sensitive than modulated technique described above.

2.4. Fluid rheology

2.4.1. Shear rheology

The test fluid was a wormlike micelle fluid, a mixture of 0.05 mol/l cetyletrimethylammonium bromide (CTAB) (Fisher Scientific) and 0.05 mol/l sodium salicylate (NaSal) (Fisher Scientific) in distilled, deionized water. The solution is well above the critical micelle concentration, which for CTAB in pure water is CMC $= 9\times10^{-4}$ mol/l [8]. At these concentrations, the wormlike micelle solution is concentrated and entangled with significant number of entanglement points per chain [8]. The FIB measurements were aided by the extremely large value of the stress-optic coefficient of CTAB surfactant solutions which facilitate accurate measurements of even small changes in the anisotropy of the wormlike micelle conformation. Following the work of Shikata et al. [32] the stress-optic coefficient of the wormlike micelle solution was assumed to be $C = -3.1\times10^{-7}$ Pa^{-1}. The equilibrium surface tension for each of the wormlike micelle solutions tested was assumed to be consistent with the value of $\sigma = 0.036$ N/m reported in the literature for CTAB/NaSal solutions above the CMC [41]. The solution was prepared and allowed to equilibrate at room temperature ($T = 23 \pm 1\,^\circ$C) for several days before experiments were performed.

The steady and dynamic shear rheology of the test fluid was characterized using a Bolin cone-and-plate controlled stress rheometer (Model CVO) with a 4 cm diameter and 1° cone. The micelle solutions were loaded and allowed to equilibrate at $T = 25\,^\circ$C for several minutes. The samples were not pre-sheared. In the regime of linear deformation imposed by these small amplitude oscillatory shear flows, it has been shown that wormlike micelle solutions can be accurately modeled by a Maxwell model having just one or two relaxation times [10]. In Fig. 2, the storage modulus, G', and loss modulus, G'', of the 0.05 mol/l CTAB and 0.05 mol/l NaSal wormlike micelle solution are plotted as a function of angular frequency, ω, along with the prediction of a single mode Maxwell model. The linear viscoelastic data and the single mode Maxwell model with a viscosity of $\eta_0 = 62$ Pa s, a relaxation time of $\lambda = 5.7$ s, and an elastic plateau modulus of $G_N^0 = 10.9$ Pa are in good agreement for much of the dynamic range of the micelle solution.

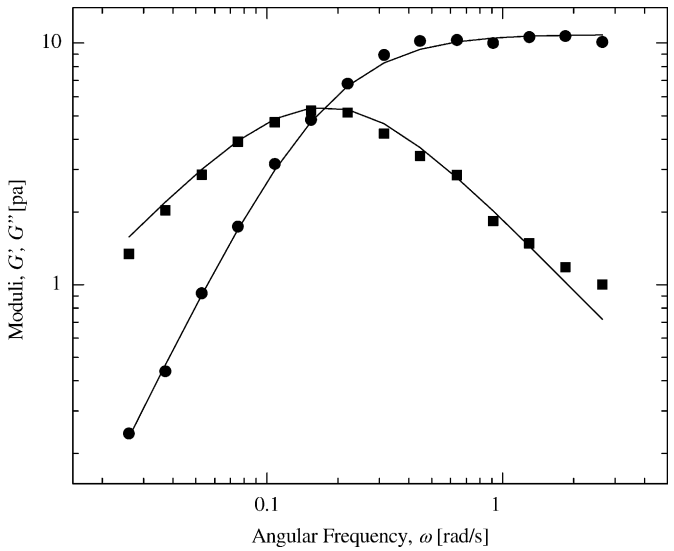

Fig. 2. Linear viscoelastic shear rheology of the 0.05 mol/l CTAB and 0.05 mol/l NaSal micelle solution. The data include: (●) the storage modulus, G'; (■) the loss modulus, G'' and (—) the fit from a single mode Maxwell model.

However, deviations are observed at large angular frequencies corresponding to the Rouse-like behavior of the micelle between entanglement points [42]. This deviation, which has been shown to become more pronounced as the concentration of surfactant and salt and therefore the number of entanglements per chain are reduced, is consistent with observations in the literature [43,44].

Although the linear viscoelasticity experiments were performed at a constant temperature of $T = 25\,^{\circ}\mathrm{C}$, the temperature in the laboratory was found to fluctuate between $T = 22$ and $24\,^{\circ}\mathrm{C}$. Thus, in order to analyze the experimental data, it was first necessary to shift the relaxation time and viscosity to their values at a reference temperature of $T_0 = 25\,^{\circ}\mathrm{C}$. This was accomplished by employing time-temperature superposition with a shift factor, a_{T}, defined by the Williams–Landel–Ferry (WLF) equation [45]. The coefficients of the WLF equation were determined to be $c_1 = 0.57$ and $c_2 = 6.94$ from linear viscoelasticity measurements of the wormlike micelle solution at a series of different temperatures.

In Fig. 3, the steady shear viscosity, η, is plotted alongside the dynamic viscosity $\eta' G''/\omega$ as a function of shear rate, $\dot{\gamma}$, and angular frequency, ω, respectively. At small shear rates and angular frequencies, the micelle solution behaves like a rheologically simple fluid; the steady and dynamic viscosity plateau to approximately the same value [45]. As the shear rate is increased, the fluid begins to shear thin. At a critical shear rate, $\dot{\gamma} \approx 2\,\mathrm{s}^{-1}$, the viscosity drops precipitously approaching a slope of $\eta \propto \dot{\gamma}^{-1}$ Although the formation of shear-banding could not be confirmed in our experiments, at similar levels of shear stress, nuclear magnetic resonance (NMR) measurements have shown the appearance of shear-banding in similar fluids [21,46]. Shear-banding could account for the dramatic reduction in the shear viscosity. The presence of shear-banding means that the flow between the cone-and-plate is no longer viscometric and the applied stress divided by the resulting shear rate is no longer a true measure of the viscosity of the wormlike micelle.

Developing and applying constitutive models that can accurately predict the rheological behavior of these wormlike micelle solutions is still a challenging issue. Superimposed over the experimental data in Fig. 3 are the predictions of several constitutive models. The solid lines in Fig. 3 represent the predictions

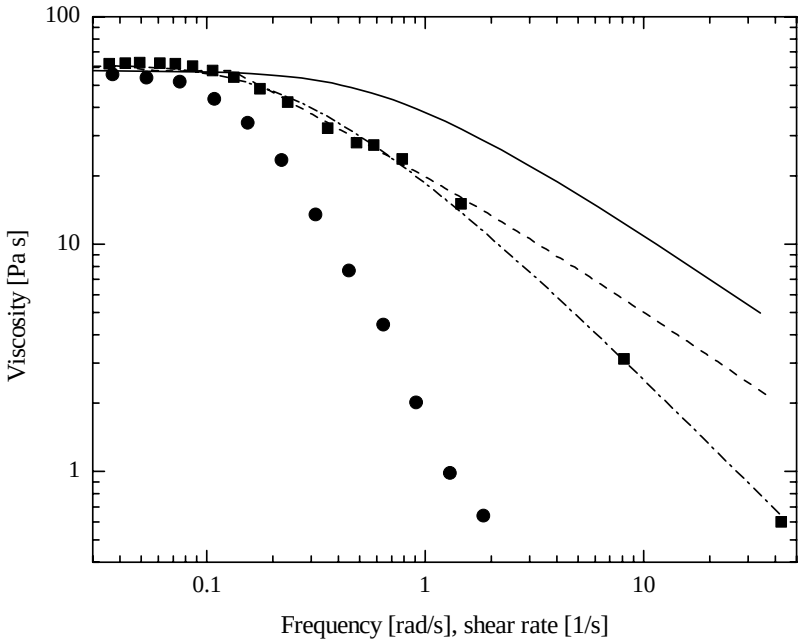

Fig. 3. Steady shear rheology of the 0.05 mol/l CTAB and 0.05 mol/l NaSal micelle solution. The experimental data include: (■) the steady shear viscosity and (●) the dynamic viscosity. The experimental data is compared to the predictions of: (—) the FENE-PM model, (- - -) the multimode Bird–DeAguiar Model and (- · -) the Giesekus model.

of a multimode FENE-PM model for the steady shear data [47]. The value of the finite extensibility parameter, $b = L^2$, used in the FENE-PM model can be computed directly from molecular quantities, thereby avoiding the need to fit the finite extensibility parameter to the shear rheology data, a practice which has been shown to result in a systematic underprediction of the finite extensibility parameter [28]. Shikata et al. [32] proposed an approximate physical model to describe wormlike micelle solutions in terms of a rubber elasticity framework. A complete discussion of the Shitaka model and its implementation can be found in [15]. The FENE-PM model does not accurately predict the onset of shear thinning in the wormlike micelle solution. However, as will be seen in Fig. 4, the FENE-PM model does an excellent job of predicting the micelle solution behavior in a transient homogeneous uniaxial extensional flow with a finite extensibility of $b = 47$ and just the first two modes of the Rouse–Zimm relaxation time spectrum are used [15].

To achieve an improved description of the shear thinning of the wormlike micelle solutions, the encapsulated dumbbell model of Bird and DeAguiar [48] was used with an anisotropic drag coefficient of $\sigma_{BD} = 0.7$, an anisotropic Brownian motion coefficient of $\beta_{BD} = 1$, and the first two modes of the Rouse–Zimm relaxation time spectrum. When $\sigma_{BD} = \beta_{BD} = 1$, the FENE-PM model is recovered. The Bird–DeAguiar model is in good agreement with the steady shear data until the onset of dramatic shear thinning. To accurately predict the slope of the viscosity at large shear rates, a model such as the Giesekus model is needed. The predictions of the Giesekus model [45] with the nonlinear parameter $\alpha = 0.15$ is also shown in Fig. 3. Unlike the FENE-PM and Bird–DeAguiar models, the Giesekus model is a good fit to the data over the entire range of shear rates. However, as will be seen in the following section, it is

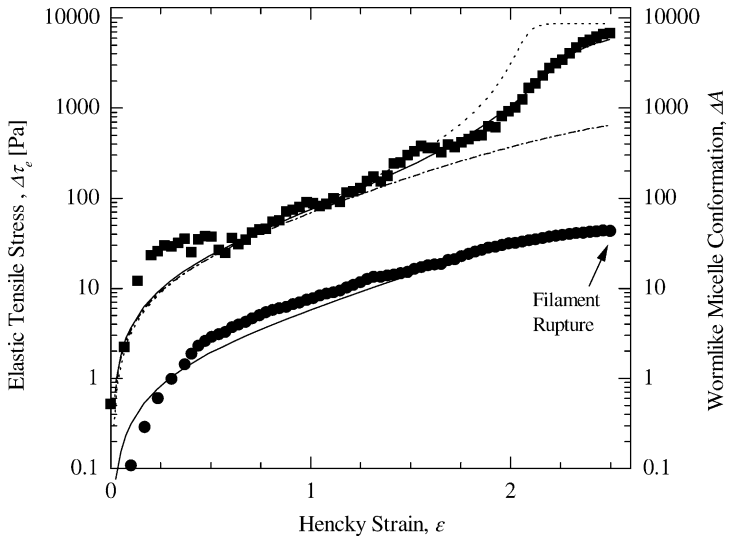

Fig. 4. Transient homogeneous uniaxial extensional rheology of 0.05 mol/l CTAB 0.05 mol/l NaSal wormlike micelle solution at a Deborah number of $De = 8.8$. The experimental data shows the growth of the tensile stress (■) and average anisotropy of the wormlike micelle (●) as a function of Hencky strain. The data is compared to the predictions of: (—) FENE-PM model and multimode Bird–DeAguiar model which are identical in extension for $\beta = 1$, (· · ·) single mode FENE-P model and (- · -) Giesekus model.

a current limitation of theory that constitutive models that can successfully predict the behavior of these wormlike micelles in shear, models like the Giesekus model and those developed by Spenley et al. [49,50] which predict an isotropic to nematic phase transition and shear-banding at a critical shear stress, fail to accurately predict the response of the wormlike micelle solution in strong extensional flows.

2.4.2. Extensional rheology

A filament stretching rheometer capable of imposing either a homogeneous uniaxial extension on a fluid filament placed between its two endplates was used to make simultaneously measurements of the evolution of the force, the midpoint radius and the FIB of the fluid filament. A complete description of the design and operating space of the filament stretching rheometer used in these experiments can be found in [33,34]. The goal of extensional rheometry is to impose a motion such that the resulting extension rate is constant

$$\dot{\varepsilon}(t) = -\frac{2}{R_{\mathrm{mid}}(t)}\frac{\mathrm{d}R_{\mathrm{mid}}(t)}{\mathrm{d}t} = \dot{\varepsilon}_0, \tag{8}$$

where $R_{\mathrm{mid}}(t)$ is the midpoint radius of the filament.

The total deformation of the system can be described in terms of a Hencky strain

$$\varepsilon = \int_0^t \dot{\varepsilon}(t')\,\mathrm{d}t' = -2\ln\left(\frac{R_{\mathrm{mid}}}{R_0}\right), \tag{9}$$

where R_0 is the initial radius of the fluid filament. The strength of the extensional flow is characterized by the Deborah number which is the ratio of the characteristic relaxation time of the fluid, λ, to the

characteristic timescale of the flow $\dot{\varepsilon}_0$,

$$De = \lambda \dot{\varepsilon}_0. \tag{10}$$

The elastic tensile stress difference generated within the filament can be calculated from the total force measured by the load cell, F_z, if the weight of the fluid and the surface tension are taken into account while ignoring inertial effects [51]

$$\langle \tau_{zz} - \tau_{rr} \rangle = \frac{F_z}{\pi R_{\text{mid}}^2} + \frac{1}{2}\frac{\rho g(\pi L_0 R_0^2)}{\pi R_{\text{mid}}^2} - \frac{\sigma}{R_{\text{mid}}}, \tag{11}$$

where L_0 is the initial endplate separation, σ the equilibrium surface tension of the fluid and ρ the density of the fluid. The principal elastic tensile stress can be further broken down into contributions from the wormlike micelles, $\Delta\tau_e$, and its Newtonian solvent

$$\langle \tau_{zz} - \tau_{rr} \rangle = \Delta\tau_e + 3\eta_s\dot{\varepsilon}, \tag{12}$$

where η_s is the solvent viscosity of the test fluid. Often the principle elastic tensile stress is nondimensionalized as a Trouton ratio, $Tr = \langle \tau_{zz} - \tau_{rr} \rangle / \eta_0 \dot{\varepsilon} = \eta_E^+ / \eta_0$, where η_E^+ is the transient extensional viscosity.

In Fig. 4, the elastic tensile stress (Eq. (12)) and the average anisotropy in wormlike micelle conformation (Eq. (1)) are plotted as a function of Hencky strain for the 0.05 mol/l CTAB and 0.05 mol/l NaSal wormlike micelle solution at a Deborah number of $De = 9.1$ and to a final Hencky strain of $\varepsilon_r = 2.7$. The tensile stress demonstrates considerable strain hardening and appears to approach an equilibrium value of the extensional stress around $\Delta\tau_e \approx 7000$ Pa. No significant contribution to the stress from the aqueous solvent is observed. The response of the wormlike micelle solution is consistent with previous filament stretching experiments of concentrated and entangled polymer melts [34,52]. The growth of the elastic tensile stress is well predicted by a multimode FENE-PM model [47] incorporating just the first two modes of the Rouse–Zimm relaxation time spectrum. In order to achieve such excellent agreement, the finite extensibility parameter of the FENE-PM model, b, was fit to the extensional data. The resulting value of $b = 47$ is within 20% of the value of $b = 55$ predicted by the approximate theory of Shikata and Kotaka [13]. The data is also well fitted by a two-mode Bird–DeAguiar model, which, because we assumed that the Brownian motion of the beads is isotropic by setting $\beta = 1$, is equivalent to the FENE-PM model. For comparison, the prediction of a single mode FENE-P model is also shown. The FENE-P model strain hardens too quickly. The Giesekus model, which did an excellent job predicting the shear rheology, significantly underpredicts the growth in the elastic tensile stress.

The average anisotropy in wormlike micelle conformation is also presented in Fig. 4. The birefringence signal is initially quite weak, but grows rapidly at short times. As time progresses and the accumulated Hencky strain increases, the anisotropy in the wormlike micelle conformation increases exponentially with time, eventually approaching an equilibrium value of roughly $\Delta A \approx 40$ which is more than 90% of the wormlike micelle's full extension. The agreement between the growth in the anisotropy in the wormlike micelle conformation and the predictions of the FENE-PM and Bird–DeAguiar models are excellent.

In order to predict the behavior of wormlike micelle solutions in both shear and extension, it appears that a constitutive model which incorporates finite extensibility into the Giesekus model is needed. Such a constitutive model was developed by Wiest [53]. Unfortunately, the use of a nonzero nonlinearity parameter ($\alpha > 0$) in the Wiest model significantly reduces the predicted extensional strain hardening of

the fluid. As a result, even with the Wiest model the shear and extensional rheology of these wormlike micelle solutions cannot be accurately predict simultaneously over the entire range of shear and extension rates. Although the two-mode Bird–DeAguiar model fails to predict the dramatic shear thinning at large shear rates, it is accurate up to shear rates of $\dot{\gamma} \approx 2\,\mathrm{s}^{-1}$ or, equivalently, Deborah numbers up to $De \approx 11$. The Bird–DeAguiar model can therefore quantitatively predict the evolution of the shear and extensional stresses for all but the largest Deborah number experiments presented in the following section, where the flow is found to be unstable. This wormlike micelle solution does not exhibit any *stress-conformation hysteresis* [54]. That is, the elastic tensile stress is found to be a single valued function of the average anisotropy in the wormlike micelle conformation. This suggests that a model such as the Bird–DeAguiar model should be capable of predicting the stable flow past a falling sphere even though the extensional flow in the wake of the sphere is inhomogeneous in nature [33].

The filament stretching experiment comes to an abrupt end at a Hencky strain of $\varepsilon_r = 2.5$ with the dramatic rupture of the fluid filament near its axial midplane. A series of high-speed images showing the rupture of the fluid filament are shown in Fig. 5. As can be seen in Fig. 5, the filament failure is not the result of elastocapillary thinning as is commonly observed in the filament stretching of weakly strain hardening polymer solutions and melts [55]. Instead, the filament experiences a rupture similar to the ductile failure of an elastic solid. The characteristic time for the breakup-recombination of these wormlike micelles, λ_{break}, has been found in the literature to be on the order of several hundred milliseconds [44]. As seen in Fig. 5, the failure of the fluid filaments occurs on much shorter timescale and thus a micelle which breaks under thermal fluctuations or the applied extensional stress will not be afforded the necessary time to reform. This filament failure therefore likely stems from the scission of wormlike micelles resulting in a dramatic breakdown of the entangle micelle network structure en masse [15]. The energy of wormlike micelle chain scission was calculated to be roughly $E_{sciss} \approx 4k_B T$ [15]. Furthermore, it has been shown by Rothstein [15] that for a series of CTAB/NaSal wormlike micelle solutions the scission energy required to break down the micelle network structure is nearly independent of both the imposed extension rate tested and the concentration of the surfactant and the salt. The failure of the wormlike micelle entangled

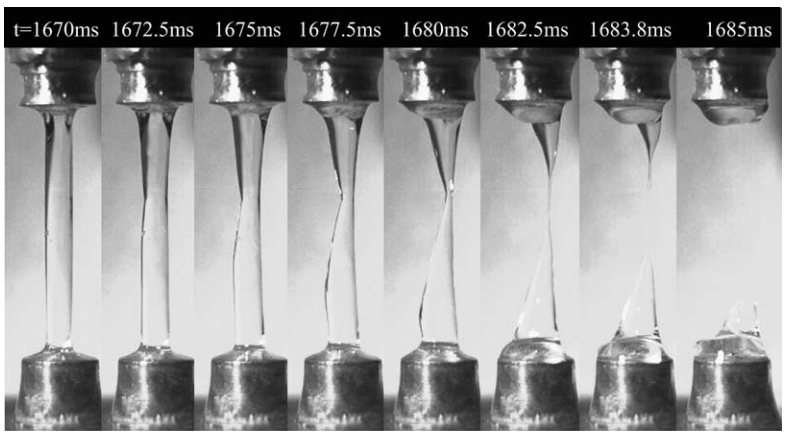

Fig. 5. Series of images showing the rupture of a filament of 0.05 mol/l CTAB and 0.05 mol/l NaSal wormlike micelle solution in a transient uniaxial extensional flow at a Deborah number is $De = 8.8$. The filament achieves a final Hencky strain of $\varepsilon_f = 2.5$ before failure.

network structure observed in these pure extensional flows can lead to new and interesting physics in complex flows such as in the extensional flow in the wake of a falling sphere.

3. Results

3.1. Sedimentation velocity

The motion of a sphere falling through an unbounded reservoir of a Newtonian fluid at zero Reynolds number was first investigated by Stokes. By balancing viscous drag with buoyancy force, Stokes was able to show that the velocity of a sphere of radius a, and density ρ_s, moving through a fluid with viscosity η_0, and density ρ_f, is given by $U_{\text{Stokes}} = 2ga^2(\rho_s - \rho_f)/9\eta_0$. Stokes' solution does not take into account the influence of the container walls, non-Newtonian effects or inertia. To quantifies the deviation in the measured terminal velocity of a sphere, U, from the predictions of Stokes flow, a drag correction factor, K, is formed [3]

$$K = \frac{U_{\text{Stokes}}}{U} = \frac{2ga^2(\rho_s - \rho_f)}{9\eta_0 U}. \tag{13}$$

In general, the drag correction factor is a function of the Deborah number, the Reynolds number, shear thinning of the fluid viscosity and the sphere-to-tube ratio, $K = K(De, Re, \eta(\dot{\gamma})/\eta_0, a/R)$.

The presence of the container tube walls will result in an additional contribution to the viscous drag thereby reducing the terminal velocity of the falling sphere. For a Newtonian fluid at zero Reynolds number, an analytical expression for the drag correction factor can be derived to account for the presence of the bounding wall [56]

$$K_N = \frac{1}{1 - f(a/R)}, \tag{14}$$

where $f(a/R)$ is the Faxen's series.

$$f\left(\frac{a}{R}\right) = 2.1044\left(\frac{a}{R}\right) - 2.0888\left(\frac{a}{R}\right)^3 + 0.9481\left(\frac{a}{R}\right)^5 + \cdots. \tag{15}$$

As seen in Table 1, for all experiments performed, the Reynolds number based on the shear rate dependent viscosity was less than $Re(\dot{\gamma}) = \rho_f U a/\eta(\dot{\gamma}) < 1$, making it possible to neglect inertial effects and placing these experiments within the creeping flow regime. The influence of rheological properties on the wall correction factor was studied by Mena et al. [57]. They were able to show that for an inelastic, shear thinning non-Newtonian fluid that the drag correction factor could be approximated by

$$K\left(\frac{a}{R}, \frac{\eta(\dot{\gamma})}{\eta_0}\right) = \frac{\eta(\dot{\gamma})/\eta_0}{1 - (\eta(\dot{\gamma})/\eta_0) f(a/R)}, \tag{16}$$

where $f(a/R)$ is again the Faxen's series from Eq. (15). No analytical expression of the drag correction factor has been developed which can also incorporate the effect of elasticity and extensional strain hardening. For such a prediction, a numerical simulation of the flow with the appropriate constitutive model is required.

A software program was developed to track the center of a sphere as it moves through a series of sequential video images. Using this program, the terminal velocity of each sphere was experimentally

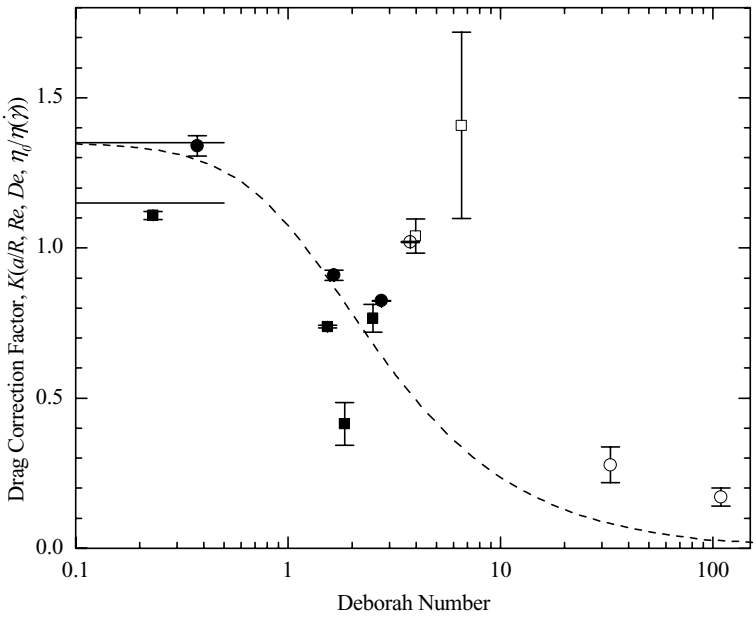

Fig. 6. The drag correction factor as a function of Deborah number for series of spheres with sphere-to-wall aspect ratios of $a/R = 0.125$ (■) and $a/R = 0.0625$ (●). The filled symbols represent stable flows while the hollow symbols represent unstable flows. The solid lines (—) correspond to the value of $K_N(a/R)$ and the dashed lines (- - -) correspond to the solution for an inelastic shear-thinning non-Newtonian fluid presented in Eq. (16).

measured. For all the stable experiments, the spheres were observed to travel along a straight path with good repeatability and no sphere rotation or movement towards the cylinder wall. In order to obtain repeatable velocity measurements, it was found that a delay of at least 10 min was needed between experiments. Failure to wait 10 min resulted in variations in the measured terminal velocities.

In Fig. 6, the drag correction coefficient is presented as a function of the Deborah number. The Deborah number was calculated from the experimentally measured terminal velocities, $De = U\lambda/a$. For experiments that demonstrated a flow instability, the Deborah number was calculated from the average sedimentation velocity. When the density of the sphere is small and the Deborah number is near zero, the observed flow behavior is Newtonian and the drag correction factor is found to approach the Newtonian theoretical limit which for the two sphere-to-tube ratios used in these experiments is calculated to be $K_N(a/R = 0.0625) = 1.15$ and $K_N(a/R = 0.125) = 1.35$. These limiting values are superimposed over the data in Fig. 6. As the Deborah number is increased, the drag correction factor decreases due to shear thinning in the fluid shear viscosity[1]. At a Deborah number of approximately $De \approx 2$, the drag correction factor reaches a minimum. Further increases in the Deborah number result in an increase of the drag correction factor. This increase is caused by the strong inhomogeneous extensional flow which develops in the wake of the sphere. The large extension rates and residence times experienced by the wormlike micelles in the wake of the sphere lead to significant micelle deformation and strain hardening

[1] The predictions for an inelastic, shear thinning non-Newtonian fluid is superimposed over the large sphere-to-tube ratio data in Fig. 6.

in the extensional viscosity as seen in Fig. 4. The extensional stresses in the wake oppose the motion of the sphere and decrease the terminal velocity. If not for these strong elastic effects the drag correction factor would decrease monotonically as predicted by Eq. (16). Further evidence of the large extensional deformation and stresses in the wake can be seen from the FIB measurements presented in Section 3.3. Similar behavior has been observed in both experiments and numerical simulation of the flow of shear thinning viscoelastic polymer solutions past falling spheres [7,58].

Above a critical Deborah number the flow becomes unstable. The symbols in Fig. 6 representing the unstable flows have been made hollow. The exact onset conditions for the flow instability could not be determined because of the discrete nature of experimentally obtainable Deborah numbers, however, the critical Deborah number appears to be approximately $De_{\text{crit}} \approx 3.8$. For both the large aluminum oxide sphere ($De = 3.8$) and the small SS sphere ($De = 4.0$), the flow was found to be stable for the majority of the experiment and was observed to exhibit between zero and two unstable flow cycles during the time it takes to pass through the flow tube. It is important to note that for both sets of spheres, the increase in the drag correction factor begins before the onset of the flow instability. As will be seen in the PIV and FIB measurements in the following sections, no significant differences were observed for the evolution of the flow past the large and small spheres. The differences observed in the evolution of the drag correction factor for the two sets of spheres arise primarily from the doubling of the sphere-to-tube ratio which results in different values of $K_N(a/R)$ and an offset in the two sets of data. One advantage of increasing the size of the spheres was that the range of Deborah number was significantly enhanced. Using the larger spheres it was possible to investigate the nature of the flow instability far from its onset conditions and to observe a maximum followed by a precipitous drop-off in the drag correction factor. If more dense small spheres were available and larger Deborah numbers could be achieved, we believe that the second downturn in the drag correction factor would be observed for both sets of spheres.

There are several physical arguments which could explain the existence of a maximum in the drag correction factor. As seen in Fig. 4, in a homogenous transient uniaxial elongational flow, the elastic tensile stress developed by the wormlike micelle solution used in these experiments approaches an equilibrium value at Hencky strains of about $\varepsilon \approx 2.5$. Further increases in Hencky strain do not result in an increase in the elastic tensile stress. The drop-off in the drag correction factor at high Deborah numbers could result from a saturation of the extensional viscosity as the wormlike micelles align with the flow and approach their finite extensibility limit. Beyond this point, even as the Deborah number and subsequently the Hencky strain accumulated by fluid elements in the wake are increased, the elastic tensile stress resisting the motion of the sphere will not increase, but remain constant. However, at these shear rates significant additional shear thinning is still possible. The combination of these two effects could result in an increase in the terminal sphere velocity and a second decrease in the drag correction factor. An alternate explanation of the maximum observed in the drag correction factor and, for that matter, the flow instability is based on the reduction in the extensional viscosity of the fluid in the wake of the sphere resulting from the scission of individual wormlike micelles and the breakdown of the entangled micelle structure. It has been theorized by Cates and Turner [16] that the distribution of micelle lengths can change under strong shear or extensional flows. This has been observed in light scattering measurements of a series of equimolar tetradecyltrimethylammonium bromide (TTABr)/NaSal solutions in a Rheometrics RFX opposed jet device which demonstrated a clear decrease in micelle radius of gyration resulting from micelle scission in the strong extensional flow [59]. This decrease in the micelle radius of gyration was found to coincide precisely with the onset of significant extensional viscosity thinning of the fluid [60]. It has also been postulated that the scission of the wormlike micelles is responsible for the experimentally observed ductile

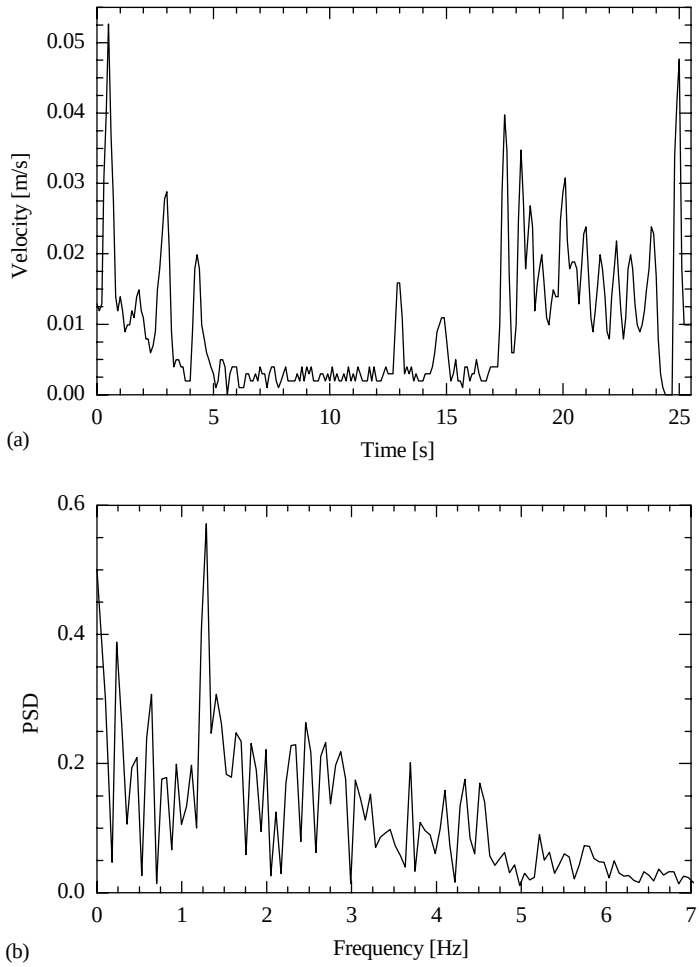

Fig. 7. The onset of a flow instability during the sedimentation of a tungsten sphere with an sphere-to-tube ratio of $a/R = 0.0625$ and a Deborah number of $De = 6.6$ as seen in: (a) measurements of the sedimentation velocity of the sphere as a function of time and (b) the power spectral density plot of the velocity fluctuations.

failure of these fluid filaments in the transient extensional rheology measurements [15]. A reduction in the extensional viscosity of the wormlike micelle solution in the wake of the sphere coupled with significant shear thinning of the fluid could also explain the observed decrease in the drag correction factor.

In Fig. 7a, the instantaneous sedimentation velocity of the unstable Tungsten sphere ($a/R = 0.0625$) at a Deborah number of $De = 6.6$ is shown as a function of time. The velocity measurements are taken far downstream of the release point of the sphere (50 cm) and are not the result of the initial transient velocity fluctuations observed as the sphere accelerates from rest [61]. Because of the large viscosity of the wormlike micelle solution, the characteristic inertial timescale for the acceleration of the sphere is very small, $\Lambda_s = 2a^2\rho_s/9\eta_0 \approx 1 \times 10^{-4}$ s [61]. This means that the transient response to acceleration is very rapid and is damped out quickly. The spheres initially fall with a steady terminal velocity. The velocity fluctuations associated with the flow instability do not grow from zero with time, but instead

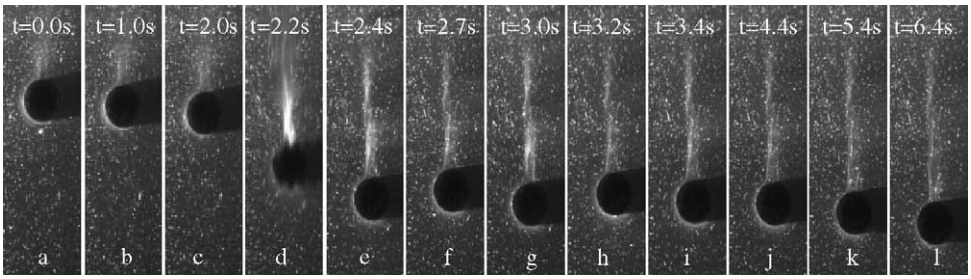

Fig. 8. A series of images showing the unstable motion of an aluminum oxide sphere with a sphere-to-tube ratio of $a/R = 0.125$ and falling with an average Deborah number of $De = 3.8$.

the fluctuations are triggered by an abrupt acceleration of the sphere. As seen in Fig. 7a, the amplitude of the velocity fluctuations is almost an order of magnitude larger than the steady terminal velocity. A fast Fourier transform was performed on the velocity fluctuation data in Fig. 7a and the resulting power spectral density plots is shown in Fig. 7b. The observed instability is clearly nonlinear with the presence of several dominant peaks, the strongest being at $f = 1.4$ Hz.

A series of images of the motion of the large aluminum oxide sphere ($a/R = 0.125$) are presented in Fig. 8 to better illustrate the flow instability. The initial motion of the sphere is stable. At $t = 2.2$ s, a flow transition occurs and the sphere abruptly accelerates. The timing and location within the fluid corresponding to the onset of the flow instability appears random and is not experimentally reproducible. After the initial acceleration, the velocity of the sphere fluctuates for several cycles. In many cases, see Fig. 8e–i, the spheres have been observed to reverse direction and move back up against gravity. Near the onset conditions, the amplitude of the velocity fluctuations typically decays with time until the fluctuations disappear. At this point, the sphere is again observed to fall with a steady terminal velocity equivalent to its initial value, see Fig. 8j–l. In some cases, as seen in Fig. 8i and j, the spheres have been observed to stop completely for nearly a second before continuing to fall. Inevitably, the sphere accelerates again and the velocity fluctuation cycle is repeated. At Deborah numbers far beyond the onset conditions, the sphere does not return to a steady terminal velocity after the initial onset of the velocity fluctuations, but remains unstable for all time. The instability has, in limited cases, coincided with significant sphere rotation and migration towards the walls of the confining cylinder.

Jayaraman and Belmonte [24] observed a similar instability in the sedimentation of a sphere through a 9 mM CTAB 9 mM NaSal wormlike micelle solutions. Jayaraman and Belmonte [24] postulated that the flow-induced structure formed in the shear regions around the sphere increased the effective viscosity of the fluid and thus the drag on the sphere. In their work, they hypothesized that the instability was due to the breakup of these flow-induced structures. However, we do not believe that this is the correct physical mechanism for the flow instability. First, shear thickening is not observed in the shear rheology of the micelle solutions used by Jayaraman and Belmonte [24] nor is it observed in Fig. 3. Second, shear thickening is typically observed before the onset of shear thinning. One would therefore expect to see a growth in drag correction factor in Fig. 6 followed by a decay. We observe the opposite trend. As will be seen from FIB measurements in Section 3.3, the increase in drag on the sphere is a result of the large extensional stresses developed within the micelle solution in the wake of the sphere. It is our hypothesis that the flow instability stems from scission of the strongly aligned and deformed micelles in the extensional

flow present in the wake of the sphere. We believe that the instability is directly related to the dramatic filament rupture observed in the extensional rheology experiments and seen graphically in Fig. 5.

In our experiments, the presence of flow-induced structure is suggested by a region of turbid fluid in the high shear regions around falling spheres with Deborah numbers above $De > 1.5$ [20]. As seen in Fig. 8, the region of turbid fluid separates from the sphere past the equator and is swept downstream. The flow-induced structure does not appear in the region of extensional flow in the wake of the sphere, remaining instead in a broad band located between one half to two radii off of the centerline. This is true even after onset of the flow instability. Upon cessation of the flow, the turbid fluid disappears within a single relaxation time, suggesting that the relaxation dynamics of the flow-induced structure is similar to the bulk fluid. In the following sections, it will be shown that the presence of the turbid fluid does not appear to affect either the velocity flow field or the FIB signal. No evidence of shear-banding or discontinuities in the velocity or birefringence signals is observed. These observations rules out the possibility of a shear-induced isotropic–nematic phase transition [62], but could be consistent with shear-induced transition to a gel-like state or another morphology [63]. To clarify the nature of the flow-induced structure transition, small angle light or neutron scattering experiments are planned in the future.

3.2. Digital particle image velocimetry

Eulerian velocity vector fields were generated using DPIV for all the spheres tested. In Fig. 9, velocity fields for a series of spheres with sphere-to-tube ratio $a/R = 0.0625$. The vectors in Fig. 9 are scaled such that an arrow of dimensionless length $l/a = 0.5$ corresponds to a dimensionless velocity of $u/U = 1$. In Fig. 9a, the velocity field around a Teflon sphere is shown at a Deborah number of $De = 1.8$. The flow has fore-aft symmetry and appears Newtonian in nature. The velocity vector field of the flow past a falling aluminum oxide sphere at a Deborah number of $De = 2.5$ is shown in Fig. 9b. At these large Deborah numbers, viscoelastic effects become important. The flow is no longer fore-aft symmetric. A weak recirculation zone is found beside the sphere and a stagnation point is observed approximately one diameter downstream of the sphere. Downstream of the stagnation point, the fluid in the wake of the sphere moves in the opposite direction of the falling sphere producing a ‘negative wake’. It has been shown through both experimentation and numerical simulation that a negative wake is present for viscoelastic fluids where the ratio of Deborah number to Trouton Ratio, De/Tr, is large [58,64]. For the wormlike micelle solution used in these experiments, the Trouton ratio asymptotes to a value of $Tr \approx 80$ resulting in a shear-rate-dependent value of $0.01 < De/Tr < 0.05$ which is well within the range fluid properties shown by Arigo and McKinley [58] to demonstrate a negative wake. For a fluid, such as a high molecular weight Boger fluid, which can demonstrate even more significant strain hardening and does not shear thin, the ratio of De/Tr, is small. Such fluids do not exhibit a negative wake, but instead they form an ‘extended wake’ [64,65]. In Fig. 9c, the velocity vector field generated by the sedimentation of a SS sphere at a Deborah number of $De = 4.0$ is shown. As the Deborah number is increased, the stagnation point moves further downstream of the sphere and the intensity of the recirculation region beside the sphere increases significantly. In addition, a considerable amount of strongly pre-sheared fluid is swept into wake of the sphere upstream of the stagnation point. As the Deborah number is increased further, the flow is found to become unstable. There is no clear evidence from these DPIV images that the turbid fluid has a significant effect on the flow. No regions of shear-banding or other flow anomalies are observed [66]. In fact, the agreement between the DPIV images obtained for these wormlike micelle solutions and those obtained for shear thinning polymer solutions that do not exhibit flow-induced structure is strong [58].

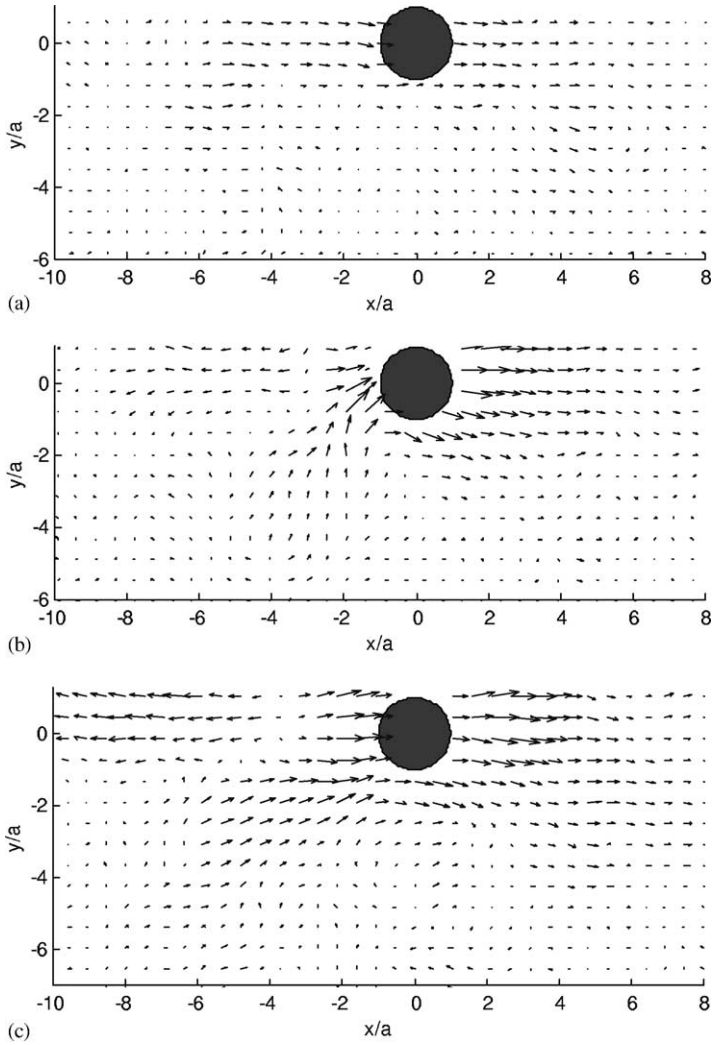

Fig. 9. DPIV vector fields of the flow past spheres with a sphere-to-tube ratio of $a/R = 0.0625$ at Deborah number of: (a) $De = 1.8$, (b) $De = 2.5$ and (c) $De = 4.0$. The sphere is moving from left to right.

To illustrate the effect of the transient motion of the spheres on the velocity flow field, a series of three DPIV images are presented in Fig. 10 for a single unstable oscillation cycle of the Tungsten sphere with $a/R = 0.0625$ falling at a Deborah number of $De = 6.6$. The DPIV images in Fig. 10 correspond to times just prior to the onset of the flow instability, during the acceleration of the sphere and during the deceleration of the sphere. The velocity vectors in Fig. 10 are scaled such that an arrow of length $l/a = 0.5$ corresponds to a velocity of $u/\bar{U} = 1$, where $\bar{U}$ is the average sedimentation velocity of the Tungsten sphere. The exact time of each of the DPIV images are highlighted on the plot of velocity fluctuations presented in Fig. 10a. Before the onset of the instability, the velocity vector field of the pseudostable flow

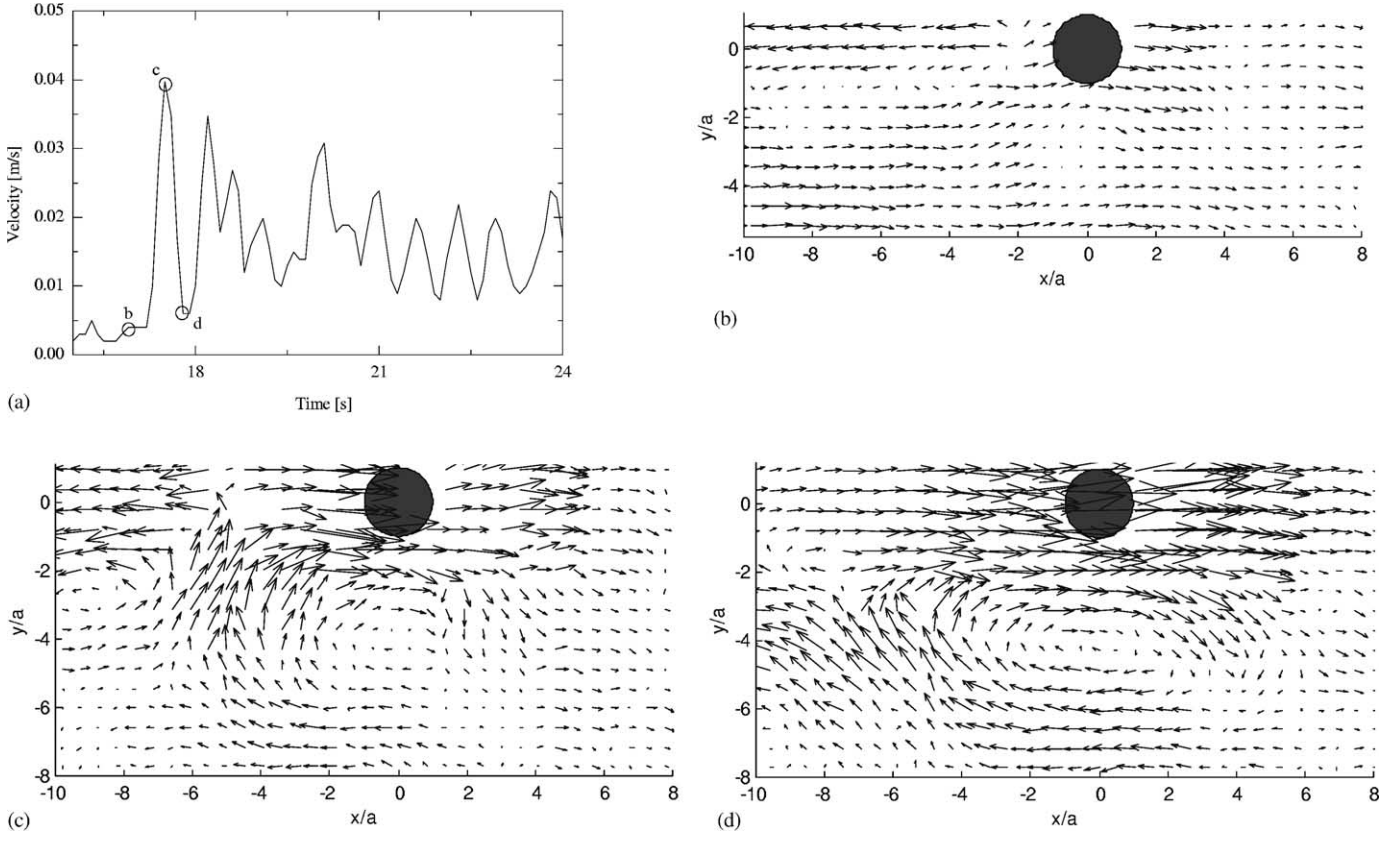

Fig. 10. Unstable sedimentation of a tungsten sphere with sphere-to-tube ratio of $a/R = 0.0625$ and an average Deborah number of $De = 6.6$. The figure includes: (a) the instantaneous velocity fluctuations as a function of time and DPIV vector fields taken during (b) pseudostable sedimentation, (c) acceleration and (d) deceleration of the sphere during a single velocity fluctuation cycle.

shows a strong recirculation pattern and the presence of a negative wake. As the sphere accelerates, the recirculation zone intensifies and the stagnation point moves further downstream to a point nearly five radii from the sphere. During deceleration, the flow is dominated by the extensional stresses generated in the wake of the sphere and the negative wake disappears in favor of an extended wake. This suggests that during deceleration De/Tr is small and the behavior of the fluid is similar to a highly elastic Boger fluid.

This behavior is quite different from observations of the transient evolution of the negative wake for sphere accelerating from rest in a shear thinning fluid [58,67]. Arigo and McKinley [58] found that the negative wake was a large strain phenomenon. During the initial stages of the transient motion of the sphere, as it accelerates from rest, neither a negative wake nor an extended wake was observed. Arigo and McKinley [58] observed that it took several cycles of the initial transient for the polymer molecules to build up enough molecular deformation and stress for the flow to exhibit a negative wake. At no point did the flow exhibit an extended wake. In our experiments, the wormlike micelles are deformed sufficiently to demonstrate a negative wake before onset of the flow instability. The DPIV measurements clearly demonstrate a transition from a shear dominated to an extension dominated flow during the completion of a velocity fluctuation cycle.

3.3. Flow-induced birefringence

The Osaki technique was used to take full-field FIB measurements for the stable sedimentation of spheres through the wormlike micelle solutions. Since this technique requires two independent measurements of the flow field, it was not possible to use this technique to measure full-field birefringence of the unstable sphere sedimentation. The technique is demonstrated in Fig. 11 for the sedimentation of an aluminum oxide sphere with an sphere-to-tube ratio of $a/R = 0.0625$ at a Deborah number of $De = 2.5$. In Fig. 9a and b, the normalized light intensity is shown for the polarizer arrangements of $0^\circ/90^\circ$ and $45^\circ/135^\circ$, respectively. The $45^\circ/135^\circ$ polarizer arrangement highlights the extensional flow in the wake and the compressive flow ahead of the sphere while the $0^\circ/90^\circ$ polarizer arrangement highlights the shear flow around the sphere. The spatially averaged values of the retardation, $\bar{\delta}$, and extinction angle, $\bar{\chi}$, were calculated from Eq. (7) and are presented in Fig. 9c and d. Strong deformation is found in the wake of the sphere where the extensional flow exists. The fluid is also strongly deformed within a region of biaxial compressive just upstream of the sphere and shear regions around the sphere. Because the flow is axisymmetric, it can be difficult to satisfactorily interpret the birefringence data, however, a qualitative description of the state of micelle deformation and stress can be garnered from the spatially averaged values of retardation and extinction angle. In addition, these spatially averaged values of the retardation and the extinction angle can then be compared directly to predictions of numerical simulations using a constitutive model of choice [37,68].

The development of the retardation and extinction angle are shown in Fig. 12 for two additional spheres with sphere-to-tube ratio $a/R = 0.0625$. The data in Fig. 12 is split such that the top have of each subfigure is the spatially averaged retardation, $\bar{\delta}$, and the bottom half of each subfigure is the spatially averaged extinction angle, $\bar{\chi}$. In Fig. 12a, the FIB measurements in the flow field around the Teflon sphere at a Deborah number of $De = 1.8$ show very little fluid deformation, only a weak shearing very close to the sphere. As the Deborah number is increased to $De = 4.0$ in Fig. 12b, a significant increase in the extensional deformation of the fluid in the wake of the sphere and the shear deformation around the sphere is observed. In none of these full-field birefringence measurements is any evidence found that indicates the region of turbid fluid is a flow-induced phase transition from an isotropic to a nematic phase. Such

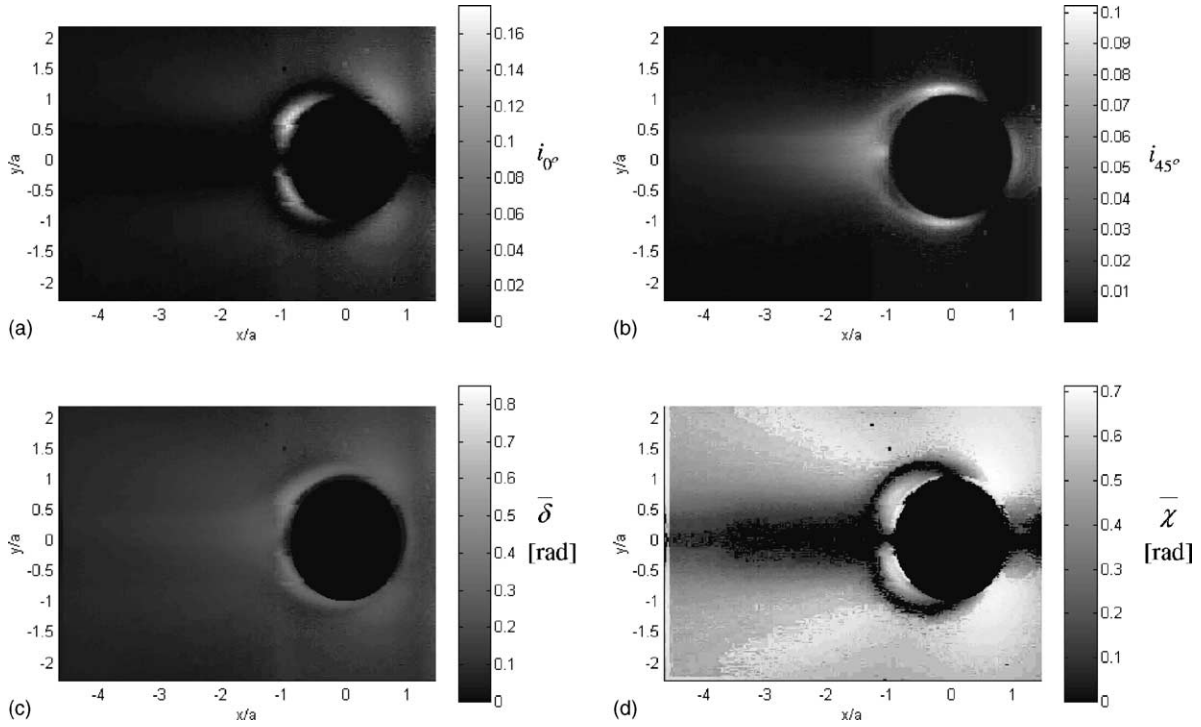

Fig. 11. Full-field FIB measurements for the sedimentation of an aluminum oxide sphere with sphere-to-tube ratio of $a/R = 0.0625$ at a Deborah number of $De = 2.5$ demonstrating the application of the Osaki technique. The figure includes: (a) normalized intensity of light for crossed linear polarizers arranged at 0°/90°and (b) −45°/45° along with the values of: (c) retardation and (d) extinction angle integrated along the line-of-sight of the interrogation laser.

a transition would result in a significantly enhanced birefringence signal from within the nematic phase. In addition, the birefringence signal from the nematic phase should decay over timescales much longer than the relaxation time of the fluid [62].

To obtain a more detailed understanding of the fluid deformation, pointwise FIB measurements were taken using the modulated technique described in Section 2.3. The path of the laser was aligned to cross the axis of the falling sphere. In each case, the extinction angle was found to align along the axis of the falling sphere such that $\bar{\chi} \approx 0°$. The results of the pointwise FIB measurements are shown in Fig. 13 for the stable spheres of both sphere-to-tube ratios. As a means of comparing with the full-field birefringence measurements in Fig. 13, the abscissa has been scaled in terms of a dimensionless distance $x/a = U/a(t - t_0)$, where t_0 is the time at which the laser is centered on the sphere.

As expected, far upstream of both the large and small spheres, the retardation is found to be vanishingly small and thus the micelles are not significantly deformed from their equilibrium conformation. Closer to the sphere, a region of positive retardation is observed. This region corresponds to a combination of both the biaxial compression and the shearing of the wormlike micelles as they approach the sphere. As the Deborah number is increased, the intensity of the fluid deformation increases and the region of influence moves further upstream. It should be noted that for many of the large sphere-to-tube ratio spheres, the FIB measurements were found to go through at least one order. The FIB signal was ‘unwrapped’ and

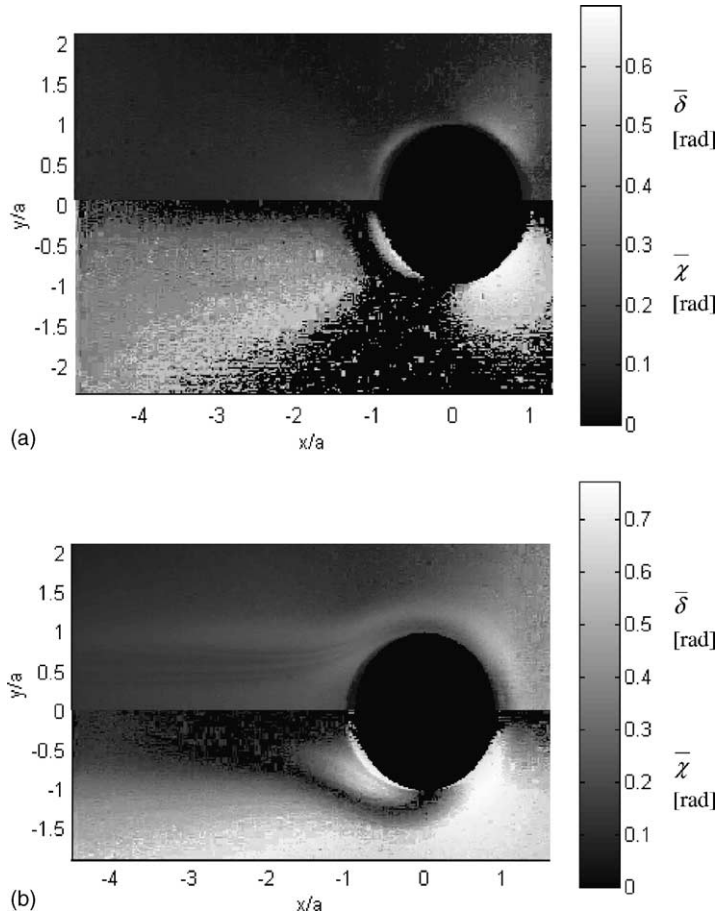

Fig. 12. Full-field FIB measurements of retardation and extinction angle integrated along the line-of-sight of the interrogation laser for the sedimentation of spheres with sphere-to-tube ratio of $a/R = 0.0625$ and Deborah numbers of: (a) $De = 1.8$ and (b) $De = 4.0$.

the resulting values of the retardation are shown in Fig. 13b. Downstream, in the wake of the sphere, a negative retardation characteristic of an extensional flow is observed. The magnitude of the spatially averaged retardation in the wake of the sphere is found to be slightly larger than the retardation upstream of the sphere. It is not possible to determine if this is a result of the spatially averaged nature of axisymmetric FIB measurement (i.e. the path length of the light through the compressed fluid is longer than through the extended fluid) or if the strength of the compressive flow upstream of the sphere is on the same order as the extensional flow in the wake. At a given Deborah number, the retardation signal is found to increase with increased sphere diameter. This is in part because of the doubling of the path length of the laser light through highly deformed fluid, but also because it can be shown that the strength of the extensional flow in the wake of the sphere grows roughly with the sphere radius, $\dot{\varepsilon} \sim a$.

At moderate Deborah numbers, the largest extension of the wormlike micelles is observed just downstream of the sphere and is found to decay smoothly with increased distance from the sphere. However,

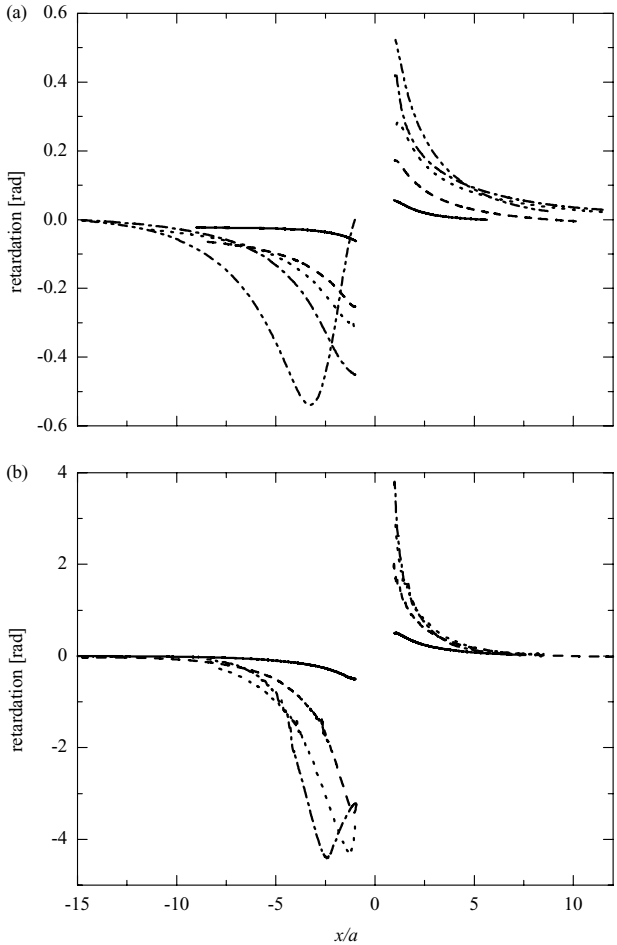

Fig. 13. Pointwise FIB measurements of retardation taken along the centerline of steady falling spheres. The figure includes: (a) spheres with a sphere-to-tube ratio of $a/R = 0.0625$ and Deborah numbers of $De = 0.23$ (—), $De = 1.5$ (- - -), $De = 1.8$ ($\cdots$), $De = 2.5$ (- $\cdots$), and $De = 4.0$ (- $\cdots$ -) and (b) spheres with a sphere-to-tube ratio of $a/R = 0.125$ and Deborah numbers of $De = 0.37$ (—), $De = 1.7$ (- - -), $De = 2.7$ ($\cdots$), and $De = 3.8$ (- $\cdots$).

at larger Deborah numbers, a maximum in the absolute value of the retardation is observed in the wake. This maximum correlates precisely to the location of stagnation point observed in the negative wake of the spheres, moving downstream with increasing Deborah number. At the stagnation point, wormlike micelles experience the largest extension rates in the flow coupled with very long residence times. The result is a significant extensional deformation. In the absence of a negative wake, the maximum extension rates occur just downstream of the sphere. Because FIB measurements are a line-of-sight technique, the retardation reported in Fig. 13 represents an integral over all the wormlike micelle microstructures along the propagation path of the interrogation laser. Thus, upstream of the stagnation point, the magnitude of the retardation decreases because the birefringence signal contains information about both the extensionally deformed fluid and the pre-sheared fluid being swept into the wake. As the stagnation point moves

further downstream and more pre-sheared fluid is swept into the wake of the sphere, birefringence just downstream of the sphere decays further, eventually even becoming positive.

For the small spheres, the magnitude of extension in the wake increases with increasing Deborah number, however, for the large spheres the retardation appears to approached an asymptotic limit of $\bar{\delta} \approx -4.5$ rad for the stable flows above $De \geq 2.7$. This suggests that the micelles in the wake of the large spheres are approaching their finite extensibility limit. Although the retardation increases only very slightly with increasing Deborah number, it is evident from Fig. 4 that as the finite extensibility limit is approached substantial increases to the tensile stress can be achieved with minimal changes to the anisotropy in the wormlike micelle conformation. As shown in Fig. 4, both the micelle deformation and stress approach a plateau at large strains. Upon reaching this plateau, no additional extensional stress can be built up in the wake of the falling spheres, however, the fluid will continued to shear thin with increasing Deborah number. This observation could explain the precipitous drop-off in the drag correction factor

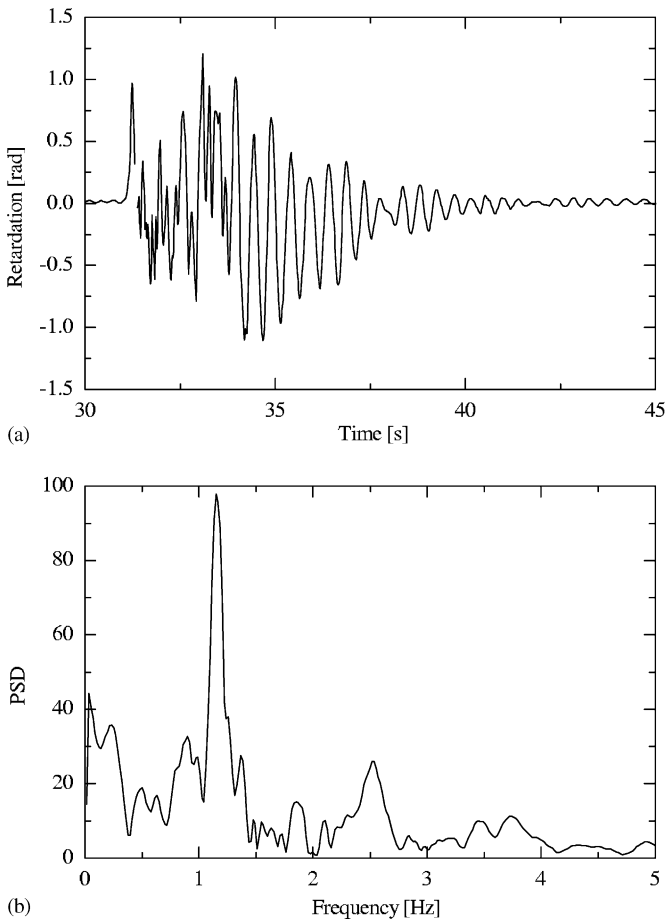

Fig. 14. FIB measurements of the unstable sedimentation of a tungsten sphere with an aspect ratio of $a/R = 0.125$ and an average Deborah number of $De = 110$. The figure includes: (a) measurements of the spatially averaged retardation in the micelle solution as a function of time and (b) the power spectral density plot of the retardation fluctuations.

observed at high Deborah numbers in Fig. 5, although it is possible that the drop-off is directly related to the onset of the flow instability. As the flow becomes unstable, the deformation in the wake of the sphere initially continues to grow towards its asymptotic limit, but for the most dense spheres the retardation is found to decay dramatically. Fig. 14 shows the retardation measured as a function of time for the tungsten sphere with $a/R = 0.125$ falling at a Deborah number of $De = 110$. The retardation signal oscillates between compressive to extensional deformation in the micelles. These deformation waves persist for some time after the sphere has come to rest at the bottom of the tank. A fast Fourier transform of the retardation signal shows a strong peak at a frequency of $f = 1.7$ Hz which is close to the strongest peak observed in the unstable sedimentation velocity measurements in Fig. 6 which were taken for the small spheres at a significantly reduced Deborah number.

4. Discussion

It is our belief that the physical mechanism responsible for the flow instability is related to the filament rupture observed in extensional rheology experiments of wormlike micelle solutions [15]. The strongest evidence for our hypothesis can be found in the full-field FIB measurements of the unstable sphere sedimentation. To highlight the regions in the flow with strong extensional deformation of the micelle, the intensity of light passing through crossed polarizer oriented at 45°/135° is shown in the wake of the unstable tungsten sphere with sphere-to-tube ratio $a/R = 0.0625$ falling with an average Deborah number of $De = 6.6$ in Fig. 15a. Because birefringence is a line-of-sight technique, quantitative calculation of microstructural deformations implicitly assume that the kinematics are homogeneous or along the propagation direction of the interrogation laser. This is clearly not true following the onset of the flow instability; and it is not possible to quantitatively measure the resulting three-dimensional variations in the microstructure. In addition, it is not possible to acquire a second image under precisely the same conditions with the polarizers reoriented at 0°/90°. The spatially averaged values of the extinction angle and the retardation thus cannot be separated unambiguously, see Eq. (6). A meaningful analysis can still be achieved if there are regions in the flow where the extinction angle is known a priori. If the extinction angle is assumed to be $\chi = 0°$ along the axis of the sphere, an assumption that is validated by the pointwise measurements, then an approximate value of the spatially averaged retardation of the wormlike micelle solution can be calculated along the axis of the sphere as a function of position in the wake of the sphere from a single intensity image. This approximate value of the retardation is presented in Fig. 15b. Unlike the retardation in the wake of all the stably falling spheres which grows and decays smoothly in the wake, the retardation in the wake of the unstably falling spheres is found to undergo a series of sharp jumps. These jumps vary in magnitude, but are found to correspond to the dominant frequency of the flow instability. Direct observations of the evolution of the wake as a function of time reveal that regions of highly birefringent material are ‘pinched off’ as the sphere accelerates and begins each new velocity fluctuation cycle. These pockets of highly deformed fluid remain in the wake of the sphere, unaffected by the continuing motion of the sphere, and their birefringence decays smoothly to zero with time [69].

We believe that the instability is the result of a breakdown or rupture of the entangled micelle network resulting from a build-up of extensional stress in the wake of the sphere which exceeds a critical value. Similar rupture dynamics were observed in the failure of wormlike micelle filaments in transient extensional rheology measurements [15]. A simple physical argument exists which can explain the flow instability and the presence of the discontinuous regions of low birefringence in Fig. 15. Although individ-

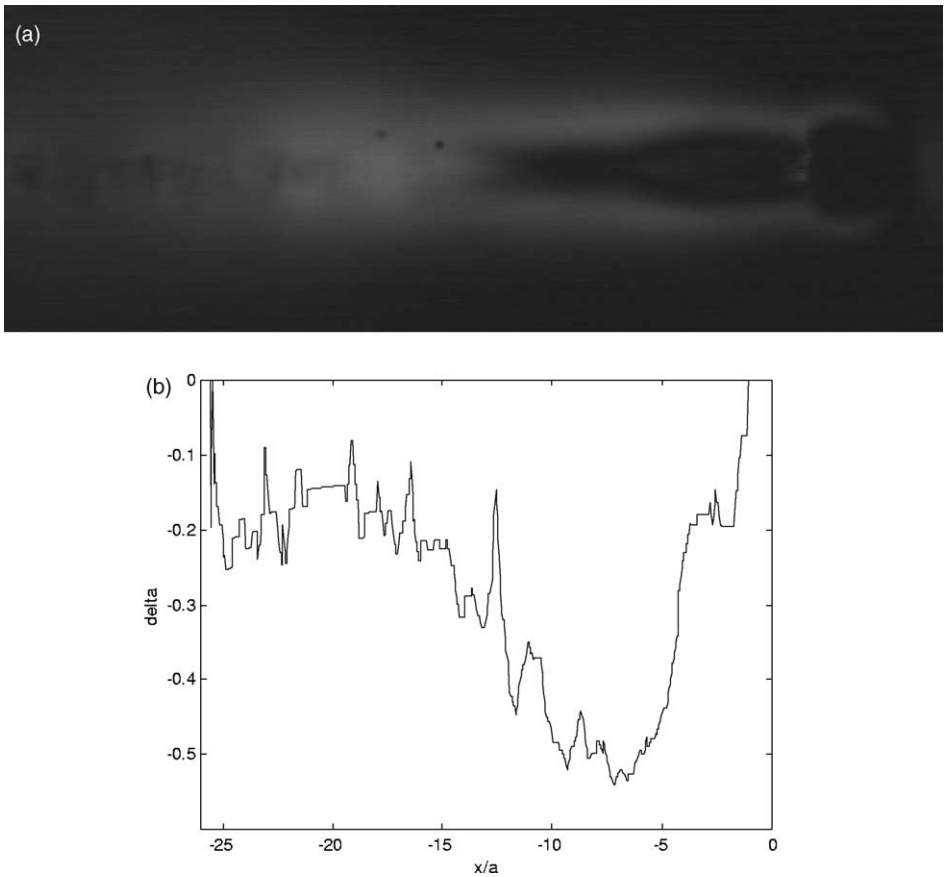

Fig. 15. Unstable sedimentation of a tungsten sphere with a sphere-to-tube ratio of $a/R = 0.0625$ and falling with an average Deborah number of $De = 6.6$. The figure includes: (a) the intensity of light passing through crossed linear polarizers arranged at $-45^\circ/45^\circ$ from the vertical and (b) the resulting retardation along the centerline of the sphere as a function of position assuming $\bar{\chi} = 0^\circ$.

ual micelles break and reform continuously under Brownian dynamics, at elevated stresses it is possible for the wormlike micelles comprising the entangled elastic network to fail en masse. The dynamics of the failure are much faster than the characteristic time for breakup and recombination of the wormlike micelles. At the point of rupture, inhomogeneous pockets of smaller wormlike micelles or even possibly spherical micelles are left behind in the wake of the falling sphere. These short wormlike micelles and/or spherical micelles contribute little to the spatially averaged retardation signal, thus accounting for the discontinuities observed in Fig. 13. In addition, once the micelle network has been ruptured it is incapable of carrying a significant extensional load. With the birefringent strand in the wake severed, the sphere accelerates. As the sphere continues to fall it passes through unaffected fluid and begins to rebuild the extensional stress in the wake. These stresses in turn decelerated the sphere until the critical rupture stress is again reached and the cycle repeats itself. This instability mechanism is further reinforced by the development of the velocity field and the disappearance of the negative wake during deceleration of the sphere.

In order to directly compare the instability observed for a falling sphere with the filament rupture observed in transient extensional rheology measurements, it would be useful to determine the maximum anisotropy in the micelle conformation in the wake of the falling sphere. Because FIB is a line-of-sight technique and the micelle conformation varies along the path of the polarized light, a qualitative estimate of the maximum conformation can only be calculated from Eq. (1) after making several key assumptions. First, the entire birefringence signal is assumed to be generated by a strongly deformed thread of wormlike micelles chains in the wake of the sphere. The full-field birefringence measurements in Figs. 9 and 10 suggest that the conformation of the wormlike micelles can be approximated to be constant and isolated within a region of thickness equivalent to one half the radius of the sphere. By substituting this assumed constant birefringence profile into Eq. (5) and integrating, a value for the FIB in the thread can be calculated in terms of the spatially averaged retardation, $\Delta n' = \bar{\delta}\lambda_{\text{light}}/\pi a$. Substituting this value of the birefringence back into Eq. (1), an expression can be derived for the maximum anisotropy in the wormlike micelle conformation as a function of the spatially averaged retardation along the centerline

$$\Delta A_{\max} \cong \frac{\bar{\delta}\lambda_{\text{light}}}{\pi a C G_0^{\text{N}}}. \tag{17}$$

The maximum anisotropy in the wormlike micelle conformation is calculated to be approximately $\Delta A_{\max} \cong 41$ for a large sphere falling with a Deborah number just below the critical conditions for the onset of the flow instability. This corresponds to more than 80% of the finite extensibility limit of the fluid and is within 5% of the critical micelle conformations observed at the point of filament rupture in transient extensional rheology [15]. Although this agreement might be fortuitous, it strongly suggests that these two flow instabilities are linked and lends additional credence to the physical mechanism put forth to explain the flow instability observed for a sphere falling through a viscoelastic wormlike micelle solution.

Acknowledgements

The authors would like to thank Gareth H. McKinley for use of his filament stretching rheometer, David Hoagland for the use of his shear rheometer, and Dr. José Bico for assistance acquiring high-speed video images, in the Matsopoulos Microfluids Laboratory at MIT.

References

[1] K. Walters, R.I. Tanner, The motion of a sphere through an elastic liquid, in: R. Chhabra, D. De Kee (Eds.), Transport Processes in Bubbles, Drops and Particles, Hemisphere Publ. Corp., New York, 1992.
[2] R.P. Chhabra, Bubbles, Drops and Particles in Non-Newtonian Fluids, CRC Press, Boca Raton, FL, 1993.
[3] G.H. McKinley, Steady and transient motion of spherical particles in viscoelastic liquids, in: R. Chhabra, D. De Kee (Eds.), Transport Processes in Bubbles, Drops and Particles, Taylor & Francis, New York, 2001.
[4] A.J. Levine, T.C. Lubensky, One- and two-particle microrheology, Phys. Rev. Lett. 85 (2000) 1774–1777.
[5] O. Hassager, Working group on numerical techniques, in: Proceedings of the Fifth International Workshop on Numerical Methods in Non-Newtonian Flows, Lake Arrowhead, USA, J. Non-Newtonian Fluid Mech. 29 (1988) 2–5.
[6] B. Yang, B. Khomami, Simulations of sedimentation of a sphere in a viscoelastic fluid using molecular based constitutive models, J. Non-Newtonian Fluid Mech. 82 (1999) 429–452.

[7] M.D. Chilcott, J.M. Rallison, Creeping flow of dilute polymer-solutions past cylinders and spheres, J. Non-Newtonian Fluid Mech. 29 (1988) 381–432.
[8] J.N. Israelachvili, Intermolecular and Surface Forces: With Applications to Colloidal and Biological Systems, Academic Press, London, 1985.
[9] R.G. Larson, The Structure and Rheology of Complex Fluids, Oxford University Press, New York, 1999.
[10] H. Rehage, H. Hoffmann, Viscoelastic surfactant solutions: model systems for rheological research, Mol. Phys. 74 (1991) 933–973.
[11] P.D. Olmsted, Dynamics and flow induced phase separation in polymeric fluids, Curr. Opin. Colloid Interf. Sci. 4 (1999) 95–100.
[12] M.E. Cates, Reptation of living polymers: dynamics of entangled polymers in the presence of reversible chain-scission reactions, Macromolecule 20 (1987) 2289–2296.
[13] T. Shikata, T. Kotaka, Entanglement network of thread-like micelles of a cationic detergent, J. Non-Cryst. Sol. 131–133 (1991) 831–835.
[14] J.W. van Egmond, Shear-thickening in suspensions, associating polymers, worm-like micelles and polymer solutions, Curr. Opin. Colloid Interf. Sci. 3 (1998) 385–390.
[15] J.P. Rothstein, Transient extensional rheology of wormlike micelle solutions, J. Rheol. 47 (5) (2003) 1227–1247.
[16] M.E. Cates, M.S. Turner, Flow-induced gelation of rodlike micelles, Europhys. Lett. 11 (1990) 681–686.
[17] M.E. Cates, Nonlinear viscoelasticity of wormlike micelles (and other reversibly breakable polymers), J. Phys. Chem. 94 (1990) 371–375.
[18] Y. Hu, S.Q. Wang, A.M. Jamieson, Rheological and flow birefringence studies of a shear-thickening complex fluid—a surfactant model system, J. Rheol. 37 (1993) 531–546.
[19] C.M. Huang, J.J. Magda, R.G. Larson, D. Pine, C.H. Liu, Shear flow rheology of micellar solutions containing 'living' polymer chains, in: Proceedings of the XII International Congress on Rheology, 1996, pp. 217–218.
[20] E.K. Wheeler, P. Fischer, G.G. Fuller, Time-periodic flow induced structures and instabilities in a viscoelastic surfactant solution, J. Non-Newtonian Fluid Mech. 75 (1998) 193–208.
[21] Y. Hu, P. Boltenhagen, D.J. Pine, Shear thickening in low-concentration solutions of wormlike micelles. I. Direct visualization of transient behavior and phase transitions, J. Rheol. 42 (1998) 1185–1208.
[22] Y. Hu, P. Boltenhagen, E. Matthys, D.J. Pine, Shear thickening in low-concentration solutions of wormlike micelles. II. Slip, fracture, and stability of the shear-induced phase, J. Rheol. 42 (1998) 1208–1226.
[23] R.G. Larson, Flow-induced mixing, demixing, and phase-transitions in polymeric fluids, Rheol. Acta 31 (1992) 497–520.
[24] A. Jayaraman, A. Belmonte, Oscillations of a solid sphere falling through a wormlike micelle solution, Phys. Rev. E 67 (2003) 065301.
[25] C. Bisgaard, Velocity-fields around spheres and bubbles investigated by laser-Doppler anemometry, J. Non-Newtonian Fluid Mech. 12 (1983) 283–302.
[26] P. Pakdel, G.H. McKinley, Digital particle imaging velocimetry of viscoelastic fluids, AIChE J. 43 (1997) 289–302.
[27] R.J. Adrian, Particle-imaging techniques for experimental fluid mechanics, Annu. Rev. Fluid Mech. 23 (1991) 261–304.
[28] J.P. Rothstein, G.H. McKinley, Extensional flow of a polystyrene Boger fluid through a 4:1:4 axisymmetric contraction/expansion, J. Non-Newtonian Fluid Mech. 86 (1999) 61–88.
[29] D. Hart, High-speed PIV analysis using compressed image correlation, J. Fluids Eng. 120 (1998) 463–470.
[30] G.G. Fuller, Optical Rheometry of Complex Fluids, Oxford University Press, New York, 1995.
[31] S. Lerouge, J.P. Decruppe, Correlations between rheological and optical properties of a micellar solution under shear banding flow, Langmuir 16 (2000) 6464–6474.
[32] T. Shikata, S.J. Dahman, D.S. Pearson, Rheo-optic behavior of wormlike micelles, Langmuir 10 (1994) 3470–3476.
[33] J.P. Rothstein, G.H. McKinley, Inhomogeneous transient uniaxial extensional rheometry, J. Rheol. 46 (2002) 1419–1443.
[34] J.P. Rothstein, G.H. McKinley, A comparison of the stress and birefringence growth of dilute, semi-dilute and concentrated polymer solutions in uniaxial extensional flows, J. Non-Newtonian Fluid Mech. 108 (2002) 275–290.
[35] P.L. Frattini, G.G. Fuller, A note on phase-modulated flow birefringence, J. Rheol. 28 (1984) 61–70.
[36] J.-M. Li, W.R. Burghardt, Flow birefringence in axisymmetric geometries, J. Rheol. 39 (1995) 743–766.
[37] J.-M. Li, W.R. Burghardt, B. Yang, B. Khomami, Flow birefringence and computational studies of a shear thinning polymer solution in axisymmetric stagnation flow, J. Non-Newtonian Fluid Mech. 74 (1998) 151–193.
[38] J.-M. Li, W.R. Burghardt, B. Yang, B. Khomami, Birefringence and computational studies of a polystyrene Boger fluid in axisymmetric stagnation flow, J. Non-Newtonian Fluid Mech. 91 (2000) 189–220.

[39] J.P. Rothstein, The stability of viscoelastic fluids in complex flows: the role of shear and extensional rheology, Ph.D. Thesis, Massachusetts Institute of Technology, 2001.
[40] G. Yu, T.Q. Nguyen, H.-H. Kausch, Birefringence of dilute PS solution in transient elongational flow, J. Polym. Sci. B 36 (1998) 1483–1500.
[41] J.J. Cooper-White, R.C. Crooks, D.V. Boger, A drop impact study of worm-like viscoelastic surfactant solutions, Colloids Surf. A 210 (2002) 105–123.
[42] P. Fischer, H. Rehage, Rheological master curves of viscoelastic surfactant solutions by varying the solvent viscosity and temperature, Langmuir 13 (1997) 7012–7020.
[43] J.-F. Berret, J. Appell, G. Porte, Linear rheology of entangled wormlike micelles, Langmuir 9 (1993) 2851–2854.
[44] A. Khatory, F. Lequeux, F. Kern, S.J. Candau, Linear and nonlinear viscoelasticity of semidilute solutions of wormlike micelles at high salt concentration, Langmuir 9 (1993) 1456–1464.
[45] R.B. Bird, R.C. Armstrong, O. Hassager, Dynamics of Polymeric Liquids. Fluid Mechanics, volume 1, Wiley, New York, 1987.
[46] M.M. Britton, P.T. Callaghan, Nuclear magnetic resonance visualization of anomalous flow in cone-and-plate rheometry, J. Rheol. 41 (1997) 1365–1386.
[47] L.E. Wedgewood, D.N. Ostrov, R.B. Bird, A finite extensible bead-spring chain model for dilute polymer-solutions, J. Non-Newtonian Fluid Mech. 40 (1991) 119–139.
[48] R.B. Bird, J.R. DeAguiar, An encapsulated dumbell model for concentrated polymer solutions and melts. I. Theoretical development and constitutive equation, J. Non-Newtonian Fluid Mech. 13 (1983) 149–160.
[49] N.A. Spenley, M.E. Cates, T.C.B. McLeish, Nonlinear rheology of wormlike micelles, Phys. Rev. Lett. 71 (1993) 939–942.
[50] N.A. Spenley, X.F. Yuan, M.E. Cates, Nonmonotonic constitutive laws and the formation of shear-banded flows, J. Phys. II 6 (1996) 551–571.
[51] P. Szabo, Transient filament stretching rheometry. I. Force balance analysis, Rheol. Acta 36 (1997) 277–284.
[52] P.K. Bhattacharjee, J. Oberhauser, G.H. McKinley, L.G. Leal, T. Sridhar, Extensional rheometry of entangled solutions, Macromolecule 35 (2002) 10131–10148.
[53] J.M. Wiest, A differential constitutive equation for polymer melts, Rheol. Acta 24 (1989) 4–12.
[54] P.S. Doyle, E.S.G. Shaqfeh, G.H. McKinley, S.H. Spiegelberg, Relaxation of dilute polymer solutions following extensional flow, J. Non-Newtonian Fluid Mech. 76 (1998) 79–110.
[55] M. Yao, G.H. McKinley, B. Debbaut, Extensional deformation, stress relaxation and necking failure of viscoelastic filaments, J. Non-Newtonian Fluid Mech. 79 (1998) 469–501.
[56] J. Happel, H. Brenner, Low Reynolds Number Hydrodynamics, Prentice-Hall, Englewood Cliffs, NJ, 1965.
[57] B. Mena, O. Manero, L.G. Leal, The influence of rheological properties on the flow past spheres, J. Non-Newtonian Fluid Mech. 26 (1987) 247–275.
[58] M.T. Arigo, G.H. McKinley, An experimental investigation of negative wakes behind spheres settling in a shear-thinning viscoelastic fluid, Rheol. Acta 37 (1998) 307–327.
[59] C. Chen, G.G. Warr, Light scattering from wormlike micelles in an elongational flow, Langmuir 13 (1997) 1374–1376.
[60] R.K. Prud'homme, G.G. Warr, Elongational flow of solutions of rodlike micelles, Langmuir 10 (1994) 3419–3426.
[61] M.T. Arigo, G.H. McKinley, The effect of viscoelasticity on the transient motion of a sphere in a shear-thinning fluid, J. Rheol. 41 (1997) 103–128.
[62] J.-F. Berret, G. Porte, J.P. Decruppe, Inhomogeneous shear flows of wormlike micelles: a master dynamic phase diagram, Phys. Rev. E 55 (1997) 1668–1676.
[63] C.H. Liu, D.J. Pine, Shear-induced gelation and fracture in micellar solutions, Phys. Rev. Lett. 77 (1997) 2121–2124.
[64] O.G. Harlen, The negative wake behind a sphere sedimenting through a viscoelastic fluid, J. Non-Newtonian Fluid Mech. 108 (2002) 411–430.
[65] M.J. Solomon, S.J. Muller, Flow past a sphere in polystyrene-based Boger fluids: the effect on the drag coefficient of finite extensibility, solvent quality and polymer molecular weight, J. Non-Newtonian Fluid Mech. 62 (1996) 81–94.
[66] M.M. Britton, P.T. Callaghan, Shear banding instability in wormlike micellar solutions, Eur. Phys. J. B 7 (1999) 237–249.
[67] D. Rajagopalan, M.T. Arigo, G.H. McKinley, The sedimentation of sphere through an elastic fluid. 2. Transient motion, J. Non-Newtonian Fluid Mech. 65 (1996) 17–46.
[68] J.P. Rothstein, G.H. McKinley, Axisymmetric flow-induced birefringence measurements for the flow of a polystyrene Boger fluid into an abrupt contraction–expansion, in: Proceedings of the XIII International Congress on Rheology, 2000.
[69] http://www.ecs.umass.edu/mie/faculty/rothstein/act_r_files/BIRE_Tungsten.avi.